Computational Geosciences

ORIGINAL PAPER

Efficient multi-scale image reconstruction of heterogeneous rocks with unresolved porosity using octree structures

Abolfazl Moslemipour[1,3] · Saeid Sadeghnejad[2] · Frieder Enzmann[1] · Davood Khoozan[3] · Thorsten Schäfer[2] · Michael Kersten[1]

Received: 9 December 2024 / Accepted: 14 April 2025 / Published online: 3 May 2025

Abstract
Identifying rock properties at the pore scale plays a crucial role in understanding larger-scale properties. For this purpose, the digital rock physics technique is used to model rock images at the pore scale. Achieving high-resolution (HR) images with a large field of view (FoV) is essential for pore-scale modeling of heterogeneous rock samples, which presents significant challenges due to their complex structures. However, because of the trade-off between resolution and FoV, it is not possible to acquire large HR images. Multi-scale image reconstruction methods enable modeling images at different resolutions and FoVs. Despite various approaches being introduced, a common limitation is the high computational cost. In this study, a novel approach based on Octree structures is introduced to minimize computational cost while maintaining accuracy. A Berea sandstone (BS) and an Edward Brown Carbonate (EBC) sample were scanned at both HR and low resolution (LR) using X-ray microtomography. Our method involves splitting the unresolved porosity in rock images into smaller sections of unresolved templates using the watershed algorithm and considering the optimized parameters. We then applied a cross-correlation based simulation technique to find the best match of each unresolved template. The novelty of our approach lies in the use of an Octree structure to perform calculations on LR images, significantly reducing computation time and memory consumption due to the fewer number of pixels in Octree LR structures. The accuracy of the images thus reconstructed using our approach was compared with those from previous methods by evaluating geometric properties and single- and two-phase flow properties. The results were promising, demonstrating that our approach achieved a permeability close to the real value, while the previous method had an error of approximately 4% for both BS and EBC rocks. More importantly, our approach was approximately three times faster and reduced memory usage by 20 to 130 times. The findings of this study facilitate dual- or multi-scale modeling and evaluate heterogeneous rock images at a significantly lower computational cost. In particular, for heterogeneous rocks, where multi-scale image reconstruction demands substantial memory and runtime, the use of the Octree technique enables accurate reconstruction with lower computational cost.

Highlights
- A rapid multi-scale image reconstruction method for rocks with unresolved porosity.
- Using an Octree structure to improve computational efficiency in image reconstruction.
- Sensitivity analysis on watershed parameters to optimize the reconstruction.

Keywords Digital twins · Microporosity · Multi resolution image · Memory consumption · Single- and two-phase properties

Computational Geosciences (2025) 29:24 https://doi.org/10.1007/s10596-025-10362-w

1 Introduction

The unbiased quantification of porous media properties is essential in various applications such as geosciences [1–6], underground hydrogen storage [7], and carbon capture and storage [8, 9]. Digital rock physics (DRP) is an effective and cost-efficient technique for predicting rock properties extracted from their images (usually CT scan-based methods) [10–13]. Many rocks worldwide exhibit highly heterogeneous structures, including tight sandstones, shales, and carbonates [14–17]. These rocks can have pore sizes at wide ranges, rendering pore modeling quite challenging. The main limitation of imaging devices such as X-ray computer microtomography (µXCT) is the trade-off between resolution and field of view (FoV). Therefore, it is not possible to obtain high resolution (HR) scans of rocks with a large FoV to accurately model the pore-scale at necessary details [2, 10, 18, 19]. Therefore, in most cases, the HR scans typically have a small FoV and are not at representative elementary volume (REV) size [10]. To address this issue, multi-scale image or pore network reconstruction techniques are introduced to resolve pore-scale details of heterogeneous rocks [20–22].

The pore network is based on the simplification of porous media to a series of pores and throats with arbitrary shapes (mostly spheres and cylinders) [23, 24]. It can preserve accuracy while reducing the computational cost [23–28]. Previous studies have introduced various multi-scale pore network reconstruction methods, including regular and upscaled approaches [18, 22, 29–32]. Prodanović et al. [30] used the Delaunay tessellation approach to randomly packed grain centers to generate a macro-pore network. Microporosity locations were then selected on the 3D images and a macro-to-micro scale ratio was defined to map a downscaled version (micro-pore network) of the macro-pore network into the selected microporosity area. The micro-pore network was then connected to the macro-pore network through throats. In a similar study, Sadeghnejad and Gostick [31] constructed dual-scale pore network in an opposite manner by adding macro-pores to a micro-pore network. They first modeled a regular equivalent pore network of a carbonate rock without vugs, and then added various numbers of vugs statistically to the system containing micropores in various realizations. These methods require high computational costs because of the presence of a large number of micropores. Moreover, one of the most significant challenges in these studies is establishing connections between scales. In further resolving this issue, Moslemipour and Sadeghnejad [18] modeled an irregular dual-scale pore network on real extracted pore networks from a carbonate sample at different resolutions. They generated a meso-scale equivalent pore network from µXCT images with a large FoV. Vugs were then added to this pore network using the extracted properties from medical-CT rock scanning. This method offers good accuracy but still requires high memory space for reconstruction and property calculation. To solve this issue, some upscaling techniques have been introduced. Bultreys et al. [32] modeled the pore network containing large and micropores by considering some "micro-links" to larger pores. The micro-links were added in the series and parallel to the macro-network. Although this approach could reduce computational costs, using the micro-link assumption still ignores some of the pore-scale complexities that influence prediction results. To address this, a recent study by Moslemipour et al. [22] introduced a multi-scale pore network reconstruction and upscaling method based on artificial neural networks. This method connects the scales using an artificial neural network, which enhances the accuracy of the reconstructed multi-scale pore networks while also reducing computational costs for property calculations by introducing an upscaling method.

In addition to multi-scale pore network reconstruction, researchers have also employed various techniques to reconstruct multi-scale images of heterogeneous rocks [33–39]. They proposed two methods for multi-scale image reconstruction: statistical and machine learning (ML). The more advanced ML approach was more recently used efficiently in different multi-scale studies and applications [40–44]. However, in multi-scale image reconstruction, ML requires extensive data and computational cost especially for large images. Therefore, statistical methods, using less data and lower computational costs, are of more practical importance [45, 46]. Okabe and Blunt [47] utilized µXCT to visualize large pores and multiple-point statistics to represent small pores, integrating them into a multi-scale porous medium model. Tahmasebi et al. [48] utilized cross-correlation-based multiple-point statistics to construct a 3D multi-scale digital model of shales, incorporating HR images for nanoscale pores and low-resolution (LR) images for large-scale pore space. They introduced a multiresolution method to reduce run time and a histogram-matching algorithm to account for concealed nanopores. In addition to these methodologies, several other studies aimed at improving the accuracy of reconstructed images in the statistical framework. Li et al. [49] presented a method for integrating HR and LR images, preserving large-scale structures but facing challenges with micro-micro connections. Jacob et al. [50] found that a REV analysis is more reliably achieved by analyzing the mean permeability variance than by analyzing the pore microstructure alone. Therefore, nanoporous domains (porous voxels) were defined in the µXCT data modeling to match better the sample permeability [51]. Additionally, the absence of assumed micro–macro connectivity introduced discrepancies in permeability results. Wang et al. [52] proposed the Local-Similarity Statistic Reconstruction method to improve pore connectivity. However, a limitation of this method was the requirement for HR and LR scans from the same location on a rock. Wu et al. [53] presented an algorithm for constructing multi-scale images of heterogeneous rock samples based on cross-correlation based simulation (CCSIM). They developed a 3D template of HR images and utilized a scan template with an overlap region (OL) on LR images to compute the cross-correlation function (CCF). The best-matched pattern from the HR template was then inserted into the LR image. In a similar study, Moslemipour et al. [54] tried to improve accuracy of the Wu et al. [53] approach by introducing the CCSIM Watershed-based Multi-scale Reconstruction (CWMR) method. This method, which considers novel overlapping areas, selects the best-matching template from the HR image for each unresolved template in the down-sampled LR image using CCF. However, it still has a high computational cost because it performs calculations on the down-sampled LR image. Due to the down-sampling of voxel size, the number of voxels significantly increases, requiring substantial memory space for storage. Additionally, performing calculations on a large number of voxels is time-consuming.

In this research, we modified the CWMR approach for multi-scale image reconstruction using the Octree structure approach, which reduces memory consumption and run time. This novel approach is then called Octree CCSIM-based Watershed Multi-scale Reconstruction (OCWMR). This is to initially segment the LR image into three distinct phases: pore, matrix, and unresolved porosity. Then, the watershed segmentation algorithm is employed to break down the unresolved regions of the image into smaller sections known as unresolved templates. For more accurate multi-scale images, a sensitivity analysis is performed on the watershed algorithm parameters. Subsequently, the voxel size of each unresolved template is down-sampled to match that of the HR image. However, the voxel size of the pore and matrix phases is preserved. This process transforms the LR image into an Octree structure. This approach significantly reduces the computational cost of reconstructing multi-scale images. Following this workflow, the CCF equation is used to find best-match templates from HR images for each resampled unresolved template. These thus selected templates are then integrated into the Octree structure. Finally, this structure is converted to a single resolution image to reconstruct the multi-scale image. With this OCWMR approach, 10 different realizations were reconstructed to estimate petrophysical and morphological image properties and validated against the reconstructed image properties using the classical CWMR approach.

The novelty of our OCWMR method, compared to previous approaches, particularly the CWMR method, lies in using the Octree structure technique, which significantly reduces memory usage and simulation runtime. Instead of performing calculations on the entire image at the finest voxel size when combining two images with different resolutions, computations are conducted on the same image utilizing an Octree structure. Specifically, watershed segmentation is applied at the larger voxel size, while template selection is performed only on the unresolved templates at the finest voxel size. Additionally, the OCWMR method employs optimal parameters for watershed segmentation, enhancing the accuracy of reconstructed multi-scale images compared to the CWMR method.

The remainder of the paper is organized as follows: Section two presents the methodology for describing the OCWMR method and its differences from the CWMR method. In the next section, we first present the REV analysis of the HR image to validate the OCWMR method. Then, we present the results of image and watershed segmentations. We then analyze the single- and two-phase flow properties of the reconstructed multi-scale images using the CWMR and OCWMR methods. It is followed by our conclusion and the main findings.

2 Methodology

The flowcharts illustrating the reconstruction of the multi-scale image using the CWMR and OCWMR methods are shown schematically in Fig. 1. Both methods start with resampling the LR image, followed by the segmentation of the LR and HR scans. In the CWMR method, the segmented LR image is down-sampled, and watershed segmentation is applied to this down-sampled image to identify the unresolved templates. Then, by solving the CCF equation on the segmented HR image, a suitable template is selected for each unresolved template in the down-sampled LR image until all unresolved templates are replaced. Finally, the multi-scale image is reconstructed. In contrast, the OCWMR method applies watershed segmentation directly to the LR image to identify unresolved templates. The voxel size is then reduced only in the unresolved templates to construct the Octree structure. By solving the CCF equation on the segmented HR image, a suitable template is selected for each

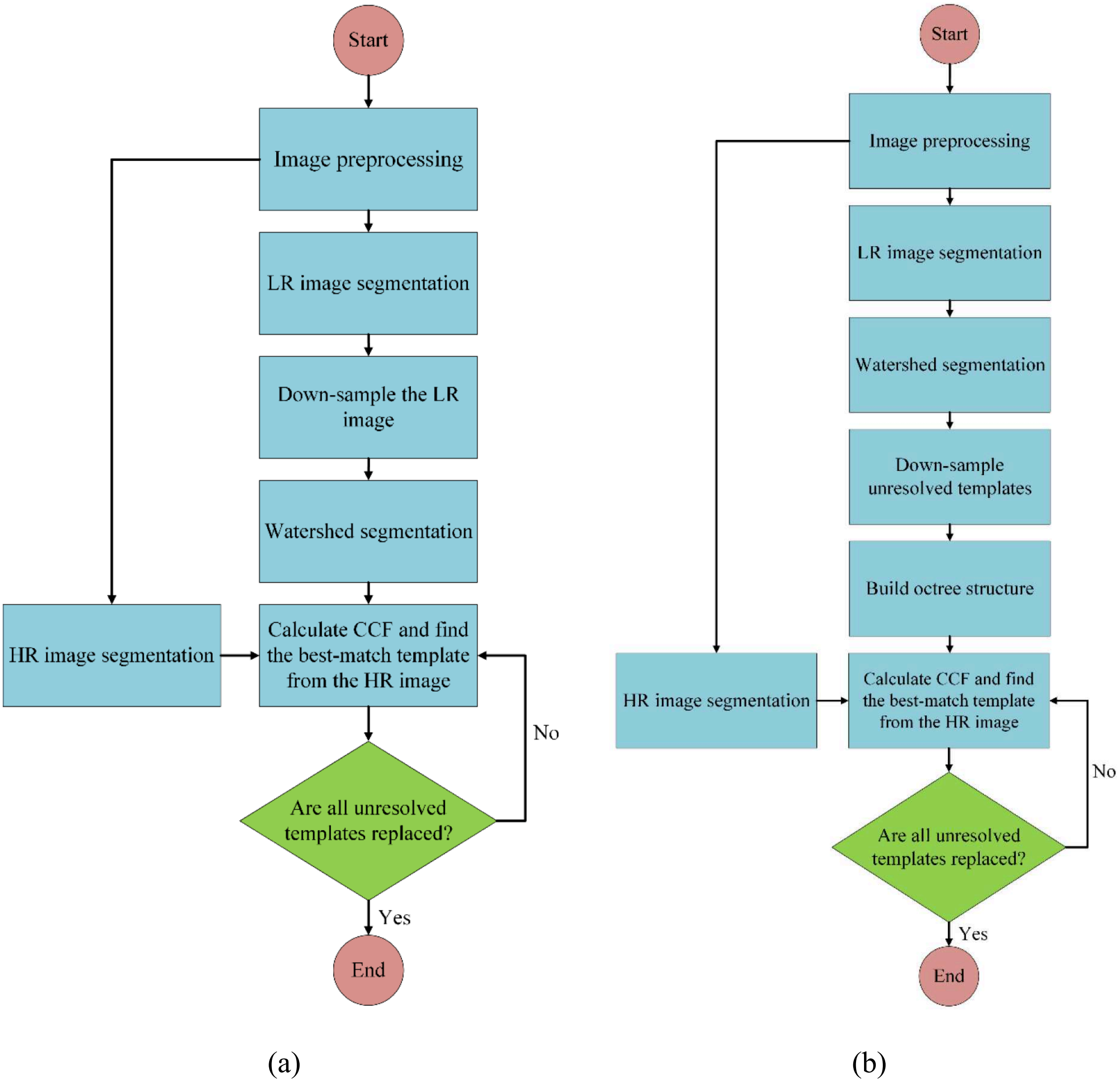

Fig. 1 Schematic flowcharts of (**a**) CWMR and (**b**) OCWMR methods

unresolved template in the Octree structure until all unresolved templates are replaced. Finally, the multi-scale image is reconstructed. More details of each step are explained in the following sections.

2.1 Pre-processing

Two well-known heterogeneous rock benchmark samples were used in this study. The first rock sample was a Berea Sandstone (BS), and the second one was an Edward Brown Carbonate (EBC). The BS rock sample was scanned at two different resolutions, 1.28 µm and 2.4 µm, respectively. In the case of the EBC rock sample, scanning was conducted at resolutions of 1.49 µm and 10.88 µm. Figure 2 shows a 2D scan from 3D grayscale images of the two rock samples. The LR and HR images of the EBC rock and the LR image of the BS rock were first scanned using a laboratory µXCT scanner [55]. Then, a computer software called X-AID (MITOS GmbH,

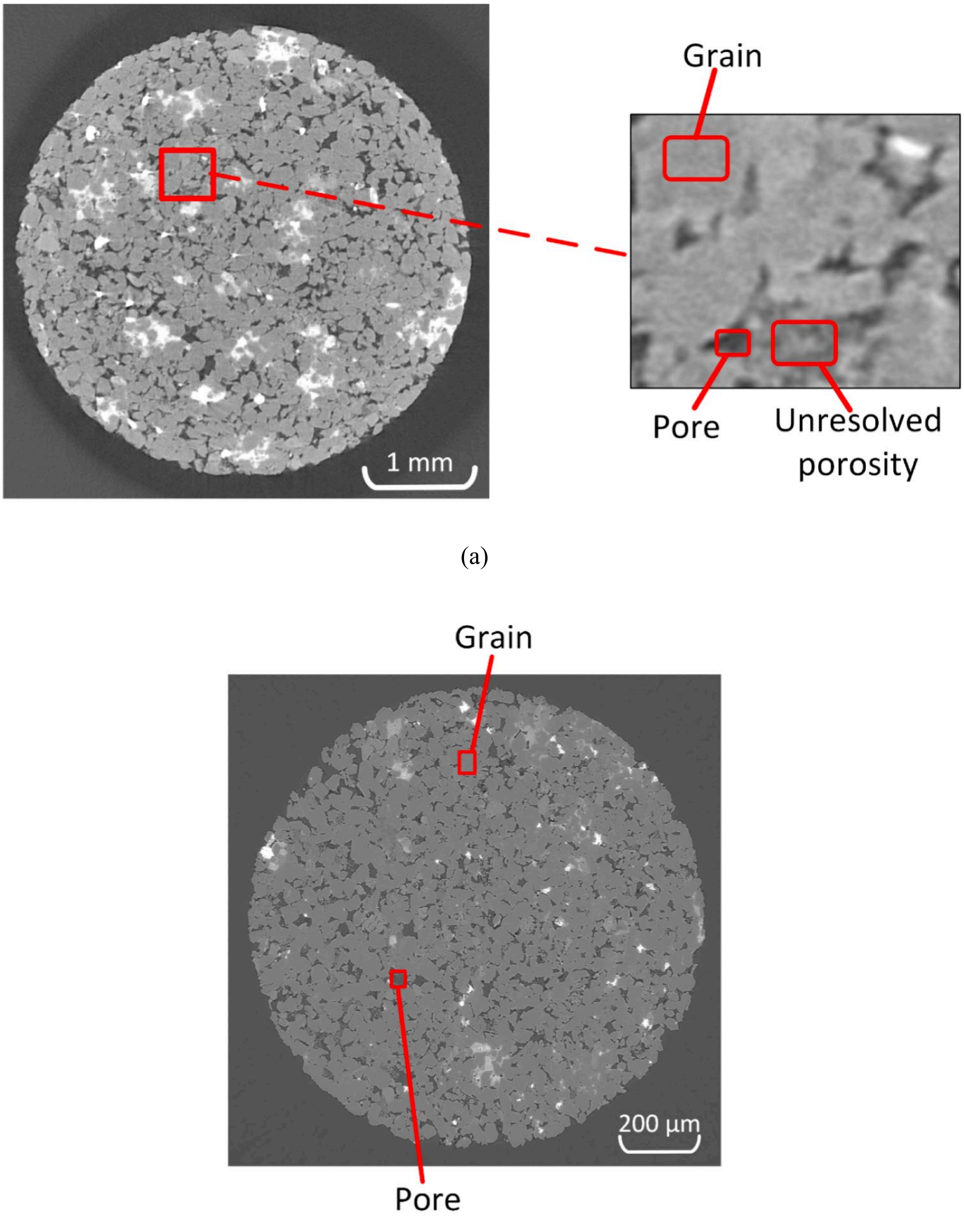

(a)

(b)

Fig. 2 A 2D scan from 3D grayscale (**a**) HR and (**b**) LR micro-CT scans of the BS rock sample, along with a 2D (**c**) HR and (**d**) LR micro-CT scans of the EBC rock sample

Fig. 2 (continued)

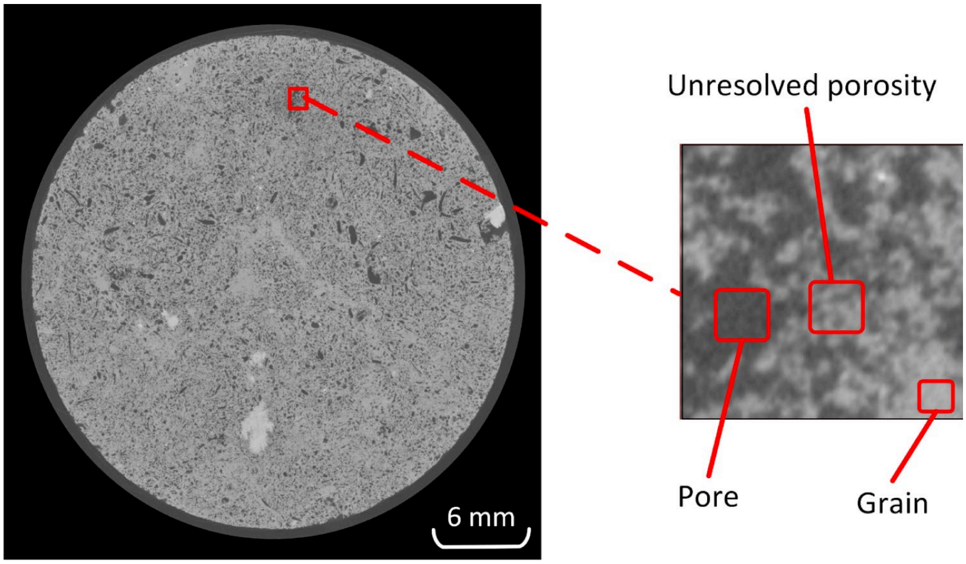

(c)

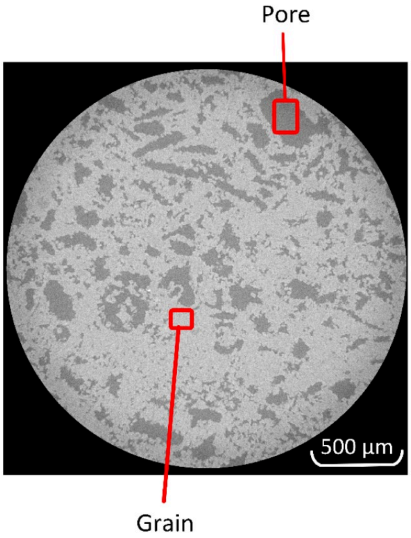

(d)

Germany) was utilized for the reconstruction, beam hardening, and ring artifact correction. The 3D image of the entire BS rock was scanned at HR of 1.28 µm using the beamline HEREON IBL P05 of the X-ray synchrotron light source PETRA III at DESY Hamburg. A sophisticated computer script written in MATLAB® was used for reconstruction and ring artifact correction in the images obtained through this synchrotron µXCT [56]. In this study, the iterative method is used for image reconstruction from images. Iterative methods significantly outperform traditional techniques such as filtered back projection in terms of reducing noise, decreasing blooming artefact, and improving the image quality [57, 58]. Moreover, ML-based approaches, once trained, can provide faster and more accurate results [59]. However, iterative methods have more usage for their robustness to different scenarios and the lack of need for large training datasets [59]. In addition, the methods to decrease ring artifacts can be classified into two main categories: sinogram processing (pre-processing techniques) and post-processing techniques [60]. ML-based methods are also used for this purpose [61]. Among the most famous methods of pre-processing and post-processing techniques, Fourier-based and median filter methods are known, respectively [60]. In this study, a Fourier-based approach was used to correct ring artifacts. This approach filters the ring patterns in the frequency domain and thus causes an effective ring artifact reduction. Compared to other simpler methods, such as median filtering, the Fourier method can reduce sharp rings of varying intensity and does not blur finer details in the image [60, 61]. Moreover, at the P05 beamline, specific settings were utilized, which were a monochromatic X-ray beam with an energy of 30 kilo-electron volts (keV), an XIMEA camera with 5,001 projections, and a binning factor of 1. Then, all scans were de-noised utilizing the non-local means method, accomplished using ImageJ version 1.52 software. Subsequently, the LR scans were cropped to dimensions of 400 × 400 × 400 voxels and 187 × 187 × 187 voxels for the BS and EBC rock samples, respectively.

After image processing, the LR images were resampled for both rock samples. This resampling is essential to combine the LR and HR scans using the Octree structure method. For this purpose, the size of the LR scan voxels was resampled so that they were 2^n times smaller than the pixels in the HR scans. To be more specific, the HR scan's pixels became 2^n times smaller, where 'n' is an integer number. We used the Bi-cubic resampling method in ImageJ version 1.52 software package. Bi-cubic interpolation maintains the structures in the images and reduces the artifact generation during the resampling process by considering 64 neighboring voxels to calculate the new voxel values. Therefore, it causes the least possible changes to the properties of the rock samples. For this purpose, the LR scan pixel size of the BS and EBC rock images were resampled from 2.40 and 10.88 µm to 2.56 and 11.92 µm, respectively. The pixel size of HR scans becomes two ($2.56\mu m = 2^1 \times 1.28\mu m \Rightarrow n = 1$) and eight ($11.92\mu m = 2^3 \times 1.49\mu m \Rightarrow n = 3$) times smaller than the pixel size of the LR scans, respectively. Therefore, the LR scan of the BS rock sample was resized from 400 × 400 × 400 voxels to 375 × 375 × 375 voxels. Similarly, the LR scan of the EBC rock sample was adjusted from 187 × 187 × 187 voxels to 170 × 170 × 170 voxels.

At the final stage, the segmentation of µXCT scan images into different phases is a crucial step in the DRP workflow [62]. This process involves segmenting the scanned image into different parts or regions based on the gray value of pixels. HR scans were thus segmented into pore and grain phases. However, segmenting the LR image was more challenging due to the presence of unresolved voxels. Our spatial resolution was larger than the small-scale size of the pores in the rock, so this imaging method could not capture them at this resolution. Therefore, in the LR image, an additional phase called unresolved porosity needs to be segmented in addition to the pore and matrix phases. HR and LR scans were segmented using a supervised artificial intelligence technique within the GeoDict 2023 software package (Math2Market GmbH, Kaiserslautern, Germany). In this software, a supervised deep learning network model called UNet is used for segmentation. The user annotate (or paints) thereby a series of labels directly onto the image, which are then provided as training data for the UNet network segmenting the original images based on these inputs. The more training data are provided to the UNet model, the better is its ability to segment pixels accurately [63]. The resulting output was segmented two phase HR images or three phase LR images. The third phase in the LR images was unresolved porosity. It's crucial to accurately label the boundary voxels between phases, as this significantly impacts the quality of the reconstructed images at multiple scales. The training utilized a window size of 52 × 52 × 52 voxels^3 with a stride of 6 in each direction. The number of features in the first and second layers were 16 and 32, and the training process consisted of 10 epochs.

2.2 CWMR

The CWMR approach was already used by Moslemipour et al. [54] to construct a multi-scale image. The basis of this approach was the construction of multi-scale images using watershed segmentation and the CCF equation for selecting the best-match templates from HR images. This approach was somewhat modified compared to the other approaches, which improved the results and further reduced the computational cost. In this approach, first the LR image was down-sampled and the unresolved porosity was divided into smaller parts (unresolved mask) using the watershed segmentation method. The watershed segmentation started by using a Gaussian filter with a sigma value of 0.4 to identify the local minima points in the image. Next, the distance transform was calculated and a maximum filter was applied with a spherical shape radius of $r_{\max} = 4$ to the image. By comparing the values obtained from these two processes, the peaks were determined. Figure 3a shows the unresolved porosity of a down-sampled LR image after watershed segmentation in which the unresolved porosity is divided into smaller regions (named unresolved masks) shown by different colors. In Fig. 3b, a small section of the image after watershed segmentation is zoomed, which contains six unresolved clusters shown by red color shapes. Figure 3c shows the cube placed around each of these unresolved masks and named as "unresolved template".

Applying the watershed segmentation and using the unresolved templates concept can reduce the computational cost for multi-scale image reconstruction using CWMR. Then, the CCF equation (Eq. 1) was used to find the best-match template for each of these unresolved templates:

$$C(i,j;x,y) = \sum_{x=0}^{l_x-1}\sum_{y=0}^{l_y-1} DI(x+i,y+j)D_T(x,y) \tag{1}$$

where $0 \le i < L_x + l_x - 1$ and $0 \le j < L_y + l_y - 1$. DI(x, y) represents the location at point (x, y) of DI of size $L_x \times L_y$, with $x \in \{0,\ldots,L_x-1\}$ and $y \in \{0,\ldots,L_y-1\}$. An OL region of size $l_x \times l_y$ and a data event D_T are used to match the pattern in the DI. To solve the CCF equation on the HR image, a new process is used to select the OL on the LR image, which is the overlap region between the current and previous unresolved templates. This caused the connectivity in the unresolved templates to be better preserved and the final reconstructed image had a higher accuracy. Moreover, OLs were selected in two perpendicular directions and their size was also considered based on the placement of unresolved templates.

Figure 4 illustrates the OL selection process for unresolved templates in CWMR. There are two possibilities to select OL. In the first case, which is shown in Fig. 4a on the left, the two unresolved templates have an OL that is rectangular in shape. On the other hand, in the second case shown in Fig. 4b, the two unresolved templates do not overlap with each other and it is a straight line. In both cases (Fig. 4a and b), dimensions of the first and second unresolved templates ($w_1 \times h_1$ and $w_2 \times h_2$) were identified. The OL for the first template consists of two adjacent regions marked in blue. The direction of OL selection depends on the positioning of the next unresolved template relative to the current one. For subsequent templates, main and secondary OLs are defined based on whether the templates overlap. In the case of overlap (Fig. 4a), the main OL depicted in red encompasses the overlapping region's width ($w\prime$) and the height of the second template (h_2), while the secondary OL (in green) has a height of

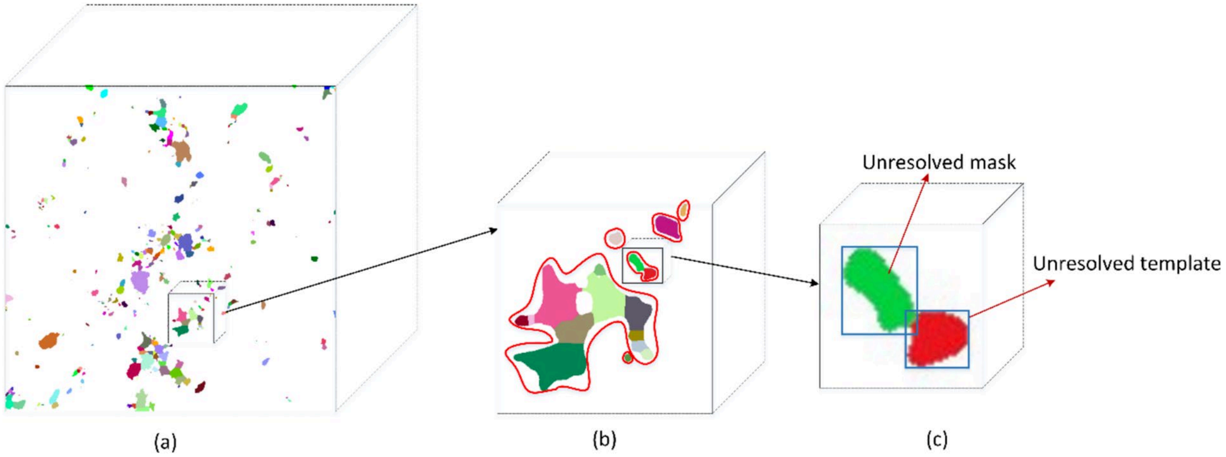

Fig. 3 Unresolved mask and unresolved template of the unresolved section after applying the watershed algorithm. (**a**) The unresolved porosity of a down-sampled LR image after watershed segmentation, which contains different unresolved masks shown by different colors. (**b**) A crop of the LR image is shown, which contains six unresolved clusters shown by red color shapes. (**c**) One of the unresolved clusters consists of two unresolved masks. Two blue line rectangles outside of each unresolved mask mark unresolved templates

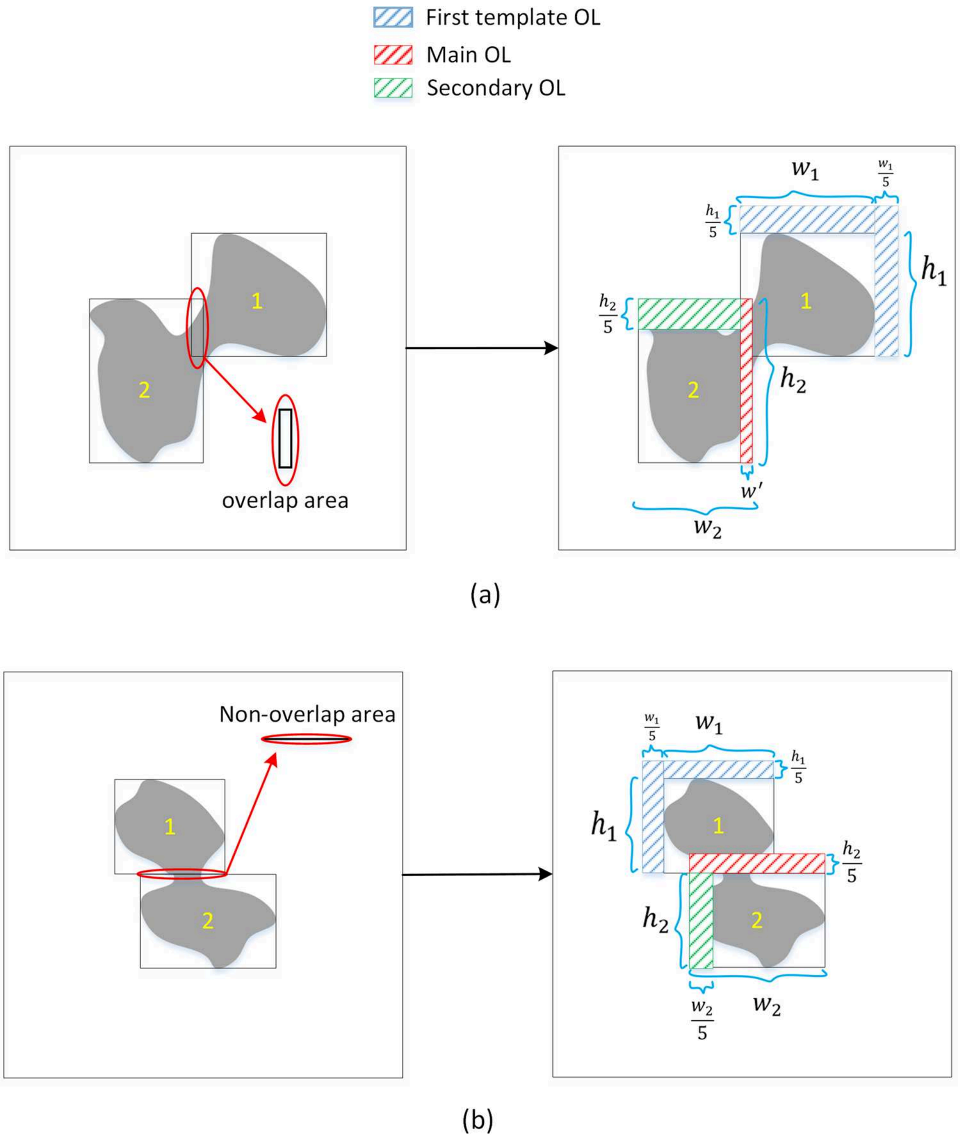

Fig. 4 Selection of OL in the CWMR approach for unresolved templates as marked by colored rectangles. The OLs of the first unresolved template are colored in blue, while those for subsequent templates are marked with main (red) and secondary (green) OL rectangles. In cases where templates overlap (**a**), the main OL aligns with the greatest contact's direction, matching the width of the overlapping region. A secondary OL is introduced, positioned in a different direction inside the second template, with a height equal to one-fifth of the second template's height. For non-overlapping templates (**b**), the main OL aligns with the greatest contact's direction outside the second template, with its height set to one-fifth of the second template's height. Simultaneously, the secondary OL, in a different direction, measures one-fifth of the second template's width

one-fifth of h_2. In non-overlapping scenarios (Fig. 4b), the main OL (still in red) has a width equal to w_2 and extends beyond the second template, with a height of one-fifth of h_2, while the vertical secondary OL is of dimension $\frac{w_2}{5} \times h_2$. This approach extends similarly to 3D images, with one main OL and two secondary OLs specified. For more details about the OL selection procedure, refer to our previous publication [54].

2.3 OCWMR

In Moslemipour et al. [54], the memory usage for multi-scale image reconstruction of two rocks was 65 GB and 276 GB, respectively. This indicates that memory consumption remained significantly high during the CWMR reconstruction. To address this issue, we have introduced the OCWMR approach in this research, aimed at further reducing the computational cost. The OCWMR method has three key differences from the CWMR method. First, to reduce memory usage and runtime, the OCWMR method uses an Octree structure, which reduces the computational cost for selecting templates from the HR image by decreasing the number of voxels in the entire reconstructed image. In this structure, voxel size is at its finest size in unresolved areas and its coarsened size in the remaining areas of the image; therefore, it requires less memory consumption to store the model. The second key difference is on the voxel size of LR images in both algorithms during the watershed segmentation. While the CWMR method performs watershed segmentation on the down-sampled LR image with a fine voxel size (equal to the HR image), the OCWMR method performs segmentation on the original LR image. Watershed segmentation performs better on the original image because it preserves the real gradients and avoids creating artificial boundaries caused by pixel repetition. In the down-sampled image, the gradients change, potentially leading to inappropriate and stepped boundaries. Therefore, this segmentation on the original LR image voxel size is more suitable for the selection of unresolved templates to be replaced with the HR image templates, improving the accuracy of the reconstructed multi-scale image.

The last key difference between the two methods is that for the OCWMR model, we performed a sensitivity analysis on the sigma and $\mathrm{r}_{\mathrm{max}}$ parameters in the watershed algorithm to select the proper values for the reconstruction, ensuring to have logical number of unresolved templates. If the number of unresolved templates is too large, their size decreases, leading to a smaller OL area. A reduced OL area also restricts the effectiveness of the CCF equation, preventing the selection of appropriate templates from the HR image. Thus, it increases the probability of excessive small-sized pores, isolated pores, dead-end throats, and poor connectivity in the reconstructed multi-scale image. Moreover, since the selected templates from the HR image do not establish proper connectivity in the reconstructed multi-scale image, this method has a higher likelihood of containing isolated small-sized pores and dead-end throats. Conversely, if the number of unresolved templates is too low, the unresolved template sizes increase, causing the selected OL region to shift away from the unresolved mask within the unresolved template. This misalignment disrupts the effectiveness of the CCF equation, leading to suboptimal template selection from the HR image. As a result, the template selection becomes somehow random, increasing the likelihood of excessive small-sized pores and poor connectivity in the reconstructed multi-scale image. For this purpose, porosity and permeability values were calculated for reconstructed images with different sigma and r_{max} values. However, the main difference between OCWMR and CWMR was the utilization of an Octree structure. An Octree is a data tree structure in which each internal node has exactly eight children. Octrees are often used to represent a three-dimensional space by recursively dividing that space into eight equal parts (Fig. 5a) Octrees are actually equivalent to quadtrees in three dimensions [64]. In fact, the 3D space modeling is a very important operation but that takes up a lot of memory capacity in computers. Octree is a method that can display the 3D space in a lighter way by occupying less memory space [65–67].

This methodology was started with watershed segmentation on the LR image, subsequently identifying unresolved templates within the image. Note that unlike the CWMR approach, the OCWMR involves solely down-sampling the unresolved templates to ensure that their voxel sizes are equal to those of the HR image. This implementation essentially transforms the LR image into an Octree structure (as depicted in Fig. 5b). Within this structure, the unresolved porosity along with some adjacent voxels (resulting from the down-sampling of unresolved templates, which incorporates some voxels outside the unresolved porosity) exhibits the fine voxel size. Conversely, the remaining areas (of both pores and grains) are characterized by a coarser voxel size [65–67].

The next step was to select the best-match template for each unresolved template. The schematic for selecting the templates from the HR image is shown in Fig. 6, where the HR image serves as the source for template selection. In Fig. 6a, an unresolved cluster is depicted which, after watershed segmentation, is transformed into two unresolved masks or templates. Consequently, for each of these unresolved templates, an appropriate template must be chosen from the HR image. Figure 6b highlights the unresolved template area, characterized by small-sized voxels, and the OL area, characterized by larger-sized voxels owing to the inherent nature of the Octree structure. In Fig. 6b, the area inside of the unresolved template and outside of the unresolved mask as well as the OL area exhibit larger voxel size. Therefore, in the beginning (Fig. 6c) the voxel size of these areas are down-sampled to match that of the HR image. Now, with the unresolved template area and OL specified, the best template can be found using the CCF equation from the HR image, and this selected template can be placed into the first unresolved template area of the LR image (Fig. 6d). Subsequently, the same approach is applied to select the best-match template for the next unresolved templates. Figure 6e shows the areas of unresolved mask with small voxel sizes, and outside of it with larger voxel size. In this figure, the main and secondary OL areas also lie outside the unresolved template area

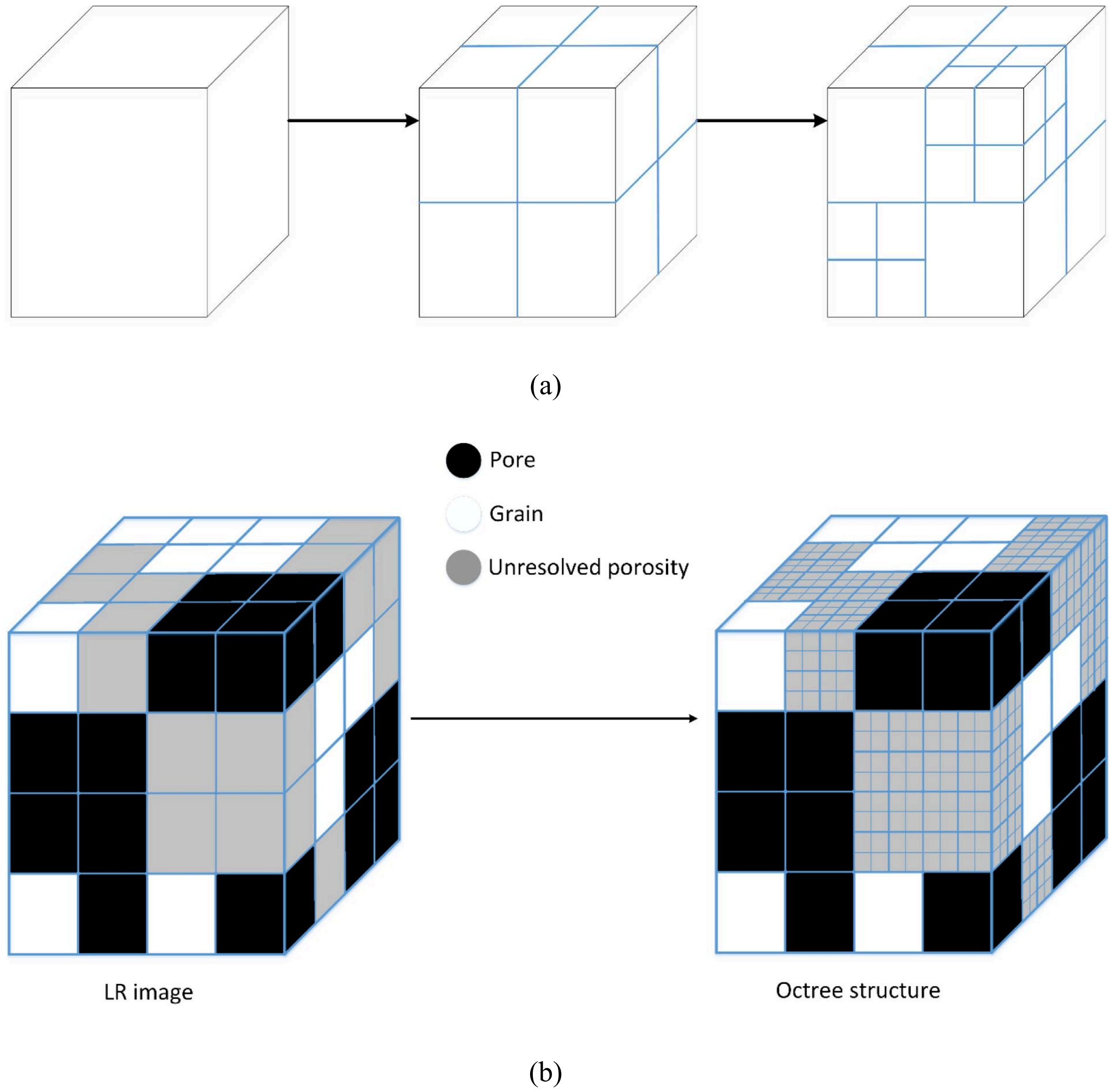

Fig. 5 **a** Octree structure and how it divides the space into smaller parts. **b** LR image to Octree structure conversion. In this structure, the voxel size is down-sampled in the areas of the unresolved porosity (the parts shown with gray color) and remains constant in the rest of the areas (black and white areas that show the pore and grain phases, respectively). Therefore, calculations are performed only in unresolved porosities with fine voxel sizes

and feature a large voxel size. Initially, the voxel size of these areas was resampled to match that of the HR image voxel size (Fig. 6f). Now, with the unresolved template area and OL defined, the best template can be selected using the CCF equation from the HR image, and this chosen template can be placed into the second unresolved template of the LR image (Fig. 6g). Finally, as depicted in Fig. 6h, the voxels within the unresolved mask were retained. This entire process was repeated for all unresolved templates within the LR image structured with an Octree structure, ultimately resulting in the construction of a multi-scale image. This innovative method introduced an efficient detour that significantly reduces computational costs through the utilization of the Octree structure.

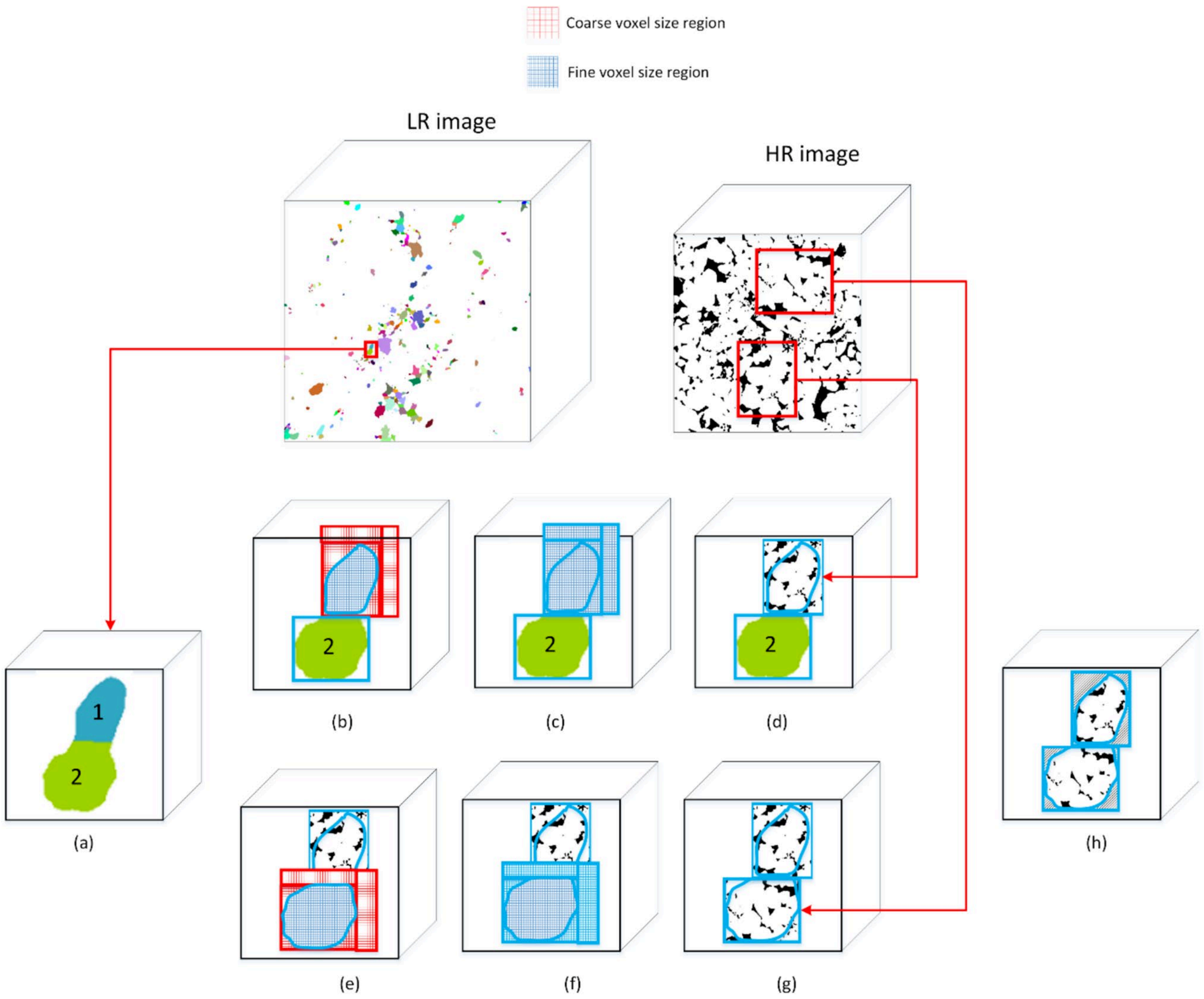

Fig. 6 Workflow of the OCWMR, (**a**) one of the unresolved clusters from the LR image with two unresolved masks inside it, (**b**) the voxel size of the first unresolved template and the corresponding OL area with large voxel size for solving the CCF equation, (**c**) the OL as well the unresolved template are resampled to the small voxel size so that it can be used in the CCF equation, (**d**) the selected best-match template from the HR image, placed within the first unresolved template, (**e**) the pixel size of the second unresolved template and the corresponding OL area with large pixel size for solving the CCF equation, (**f**) this OL as well as the unresolved template are also resampled to the small voxel size so that it can be used in the CCF equation, (**g**) the selected best-match template from the HR image as placed within the second unresolved template, and (**h**) the pixels preserved inside the unresolved templates, while the remaining pixels outside are removed, and the corresponding pixels from the LR image are placed inside (not shown here)

2.4 Geometrical and fluid flow properties

2.4.1 Porosity

Porosity is a measure to compute the total void space of a porous rock sample. The porosity of the multi-scale image is determined by dividing the number of voxels representing the pore phase by the total number of voxels (Eq. 2).

$$\phi = \frac{N_p}{N_T} \tag{2}$$

where, ϕ represents the porosity, N_p stands for the number of voxels in the pore phase, and N_T denotes the total number of voxels in the multi-scale image.

2.4.2 Absolute and relative permeability

Absolute and relative permeability are the fundamental properties of porous media that describe the capacity of a fluid to flow through a fully saturated medium. The medium's absolute permeability is determined by several rock and fluid properties, including the connected porosity, the size and connectivity of the pores and throats, the tortuosity (the degree of convolution of the flow path), and the fluid viscosity. These properties interact with each other in complex ways to determine the overall permeability of the medium. To describe the conservation of mass and momentum in such cases, the Navier–Stokes equations and the continuity equation are adopted. In this study, the software package GeoDict 2023 with adaptive meshing [68], was employed for solving these equations. The FlowDict module's Left-Identity-Right (LIR) solver was utilized employing LIR trees to optimize the efficiency of the flow solver and thus reduce computational costs [69]. This technique involves coarsening pore spaces with minimal velocity variations while maintaining a fixed resolution for other pores. The simulations in this study maintained constant pressure differentials across the domains and imposed no-flow boundary conditions in the tangential directions. Moreover, on the surfaces of solids, the no-slip boundary condition is assumed ($\vec{u} = 0$). Equation 3 states that the divergence of the velocity field ($\vec{u}$) is zero, implying that the fluid is incompressible and meaning the volume of fluid phase elements does not change as they flow:

$$\nabla.\vec{u} = 0 \tag{3}$$

Equation 4 represents the conservation of momentum and describes how the velocity field changes over time, where, $\vec{u}$ is the fluid flow velocity, p is the pressure, μ is the fluid viscosity, ρ is the fluid density, ∇ is the gradient operator, and $\vec{f}$ is the force density, connected as follows:

$$-\mu\Delta\vec{u} + \left(\rho\vec{u}.\nabla\right)\vec{u} + \nabla p = \vec{f} \tag{4}$$

Then, Darcy's law is used to compute the permeability K of the images:

$$\vec{u} = -\frac{K}{\mu}\nabla p \tag{5}$$

As mentioned, relative permeability is another basic multiphase flow property used to describe the flow behavior of fluids in porous media. It is defined as the ratio of the effective permeability of each phase in the presence of multiple fluids to the absolute permeability of the medium. In a two-phase system, the relative permeability (Kr_i) of a fluid phase i is given by:

$$Kr_i = \frac{K_{eff,i}}{K_{abs}} \tag{6}$$

where $K_{eff,i}$ is the effective permeability of phase i and K_{abs} is the absolute permeability of the medium. The relative permeability curve is typically plotted as a function of the fluid phase saturation, which is the ratio of the volume of that phase to the total pore volume of the porous medium. The SatuDict module's LIR solver of GeoDict 2023 was utilized for relative permeability calculations.

2.4.3 Capillary pressure

Capillary pressure is the pressure difference across the curved interface between two immiscible fluids in contact with each other in a small capillary tube or a porous material. The capillary pressure calculation is based on the

Young–Laplace equation and is expressed in terms of wetting and non-wetting phase pressures as expressed by Eq. 7 below:

$$\Delta P = P_{nw} - P_w = \frac{2\delta \mathrm{Cos}\theta}{r} \tag{7}$$

where, ΔP_c is the capillary pressure (in Pa units), P_{nw} is the pressure in the non-wetting phase (Pa), and P_w is the pressure in the wetting phase (Pa). Moreover, δ is the interfacial tension (IFT) between the two fluids (N/m), θ is the contact angle (degrees) between the fluid and the capillary wall, and r is the radius of the capillary (m). As indicated by Eq. 7, the capillary pressure in a reservoir is determined by various factors, including the IFT between two immiscible fluids, the contact angle between rock and fluid (θ) as influenced by the wettability of the rock, and the pore radius (r) as a microscopic property of the rock. In this study, the dynamic pore morphological method in the SatuDict module of GeoDict 2023 was utilized for capillary pressure calculations. It offers two approaches: quasi-static and dynamic methods [70, 71]. In this method, fluid flow is modeled at the pore scale using voxelized representations of the pore space. It simulates fluid invasion by progressively filling the pore space and employs morphological operations to directly calculate the fluid phase distribution in the digital twin, rather than extracting an idealized network. Dynamic pore morphological method simulates the drainage process accurately [72]. In this approach, the capillary pressure decreases as the fluid moves through a pore throat. The structure does not fill immediately, preventing abrupt transitions in the saturation region. We analyzed two-phase flow properties (capillary pressure and relative permeability) using water and air phases at varying water saturations. The wettability distribution was considered homogeneous throughout the porous medium. We fixed contact angle values at 40 degrees for water and 140 degrees for air. The surface tension was set to 0.3 N/m. Periodic boundary conditions and a pressure drop of 10,000 Pa were applied. Additionally, no-slip boundary conditions were enforced in the tangential direction.

3 Results and discussion

3.1 REV analysis

In this study, the properties of the reconstructed multi-scale images were validated against those obtained from the HR image. However, in practice, HR images typically have a small FoV and are not at REV size. At REV size, image properties represent the macroscale features of the sample rock [55, 73]. To ensure our model accuracy, we have tried to scan our two rock samples at a resolution in which the HR image be at its REV size. The deterministic REV method was used, in which porosity and permeability were calculated for the regions of interest within cubic domains of increasing size from the center of the images [18]. Figure 7a and b show the REV results for BS and EBC rocks, respectively. Moreover, the plotted mean and the associated standard deviation lines are shown in this figure. According to Fig. 7a, for the BS rock, porosity values stabilize at 300 × 300 × 300 voxels, while permeability values stabilize at 600 × 600 × 600 voxels. Moreover, in Fig. 7b, for the EBC rock, porosity values stabilize at 500 × 500 × 500 voxels, and permeability values reaches to its REV at 1,100 × 1,100 × 1,100 voxels. Therefore, for the BS rock, we selected a 600 × 600 × 600 voxels crop from the HR image. For the EBC rock, we selected a 1,100 × 1,100 × 1,100 voxels crop from the HR image.

3.2 LR and HR image segmentation

Our methodology involved two segmentation steps: HR image segmentation and LR image multi-phase segmentation. The first step consisted of a two-phase segmentation of HR images, separating just pore and grain phases. The porosity calculation for BS and EBC rock samples in the HR images yielded values of 13.7% and 28.2%, respectively. The second step consisted of a multi-phase segmentation of the LR image, revealing porosities of

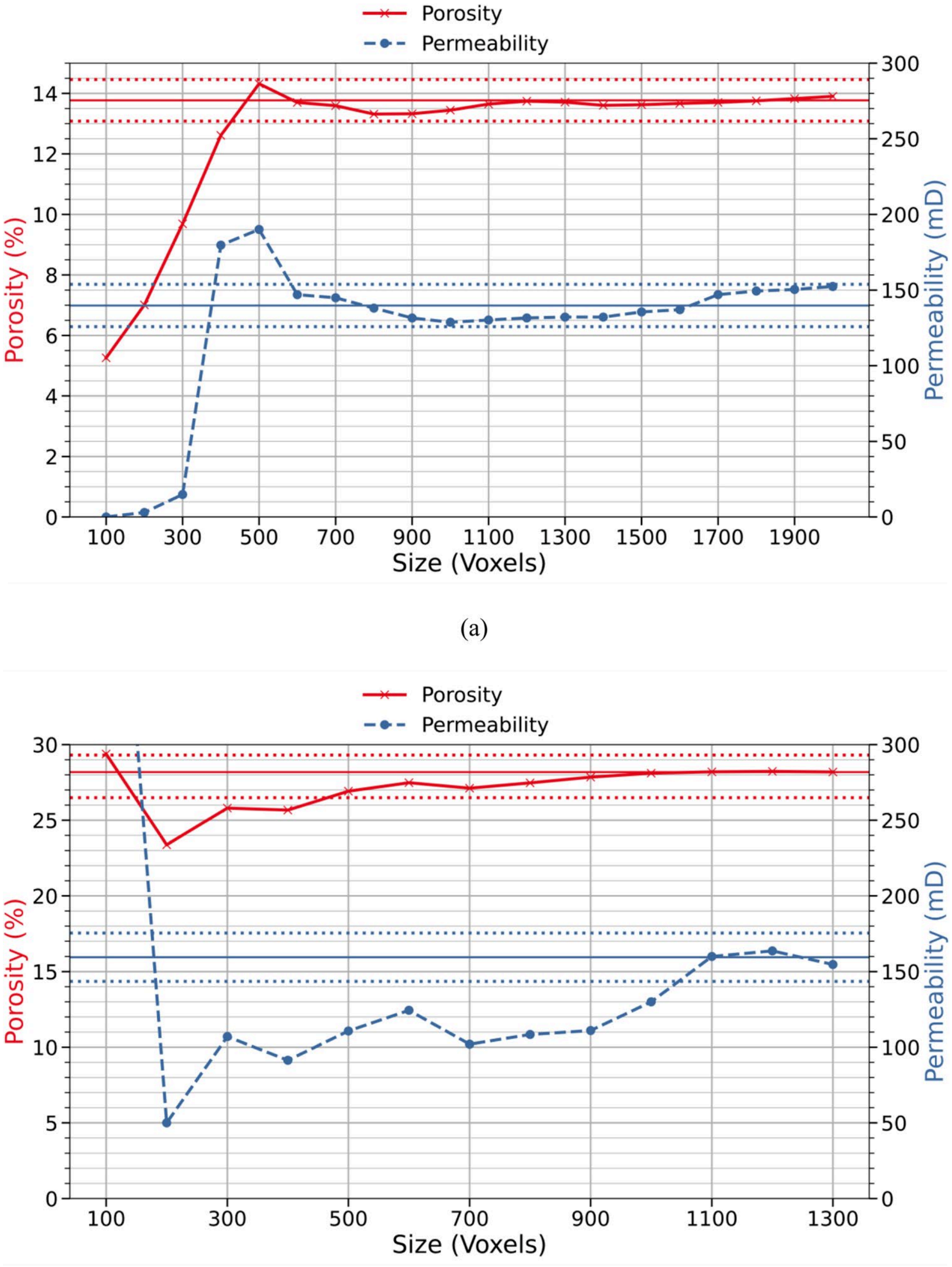

Fig. 7 REV curves of the HR images for (**a**) BS and (**b**) EBC rock samples. The dashed lines represent the standard deviation of the endpoints in the curves

(a)

(b)

12.9% and 9.3% for the pore and unresolved phase in the BS rock sample, and 21.0% and 22.6% for the pore and unresolved phase in the EBC rock sample, respectively. Table 1 represents the porosity and permeability values of the LR and HR images. Discrepancies in porosity values between LR and HR images were due to the presence of unresolved phases, which would be replaced by the best-match unresolved templates from the HR image. Moreover, segmented LR and HR images are depicted in Fig. 8.

The porosity of the unresolved phase is 9.3% in the BS rock and 22.6% in the EBC rock. This is due to the greater resolution difference between LR (11.92 µm) and HR (1.49 µm) images in the EBC rock causing many pores uncaptured and unresolved during imaging. According to Table 1, the permeability of the HR image was 160 mD, while it was only 94 mD for the LR image. On the contrary, for the BS rock, the permeability of the

HR image was lower with 147 mD than of the LR image with 170 mD. Therefore, the addition of unresolved pores in the EBC rock has a greater effect on image properties (especially permeability) because of their greater porosity than the BS rock.

3.3 LR image watershed segmentation

In addition, the watershed algorithm was used to partition unresolved porosity phase in the LR image into smaller regions. Unlike the CWMR approach, the watershed algorithm was performed on the LR image with a large pixel size. Therefore, we expect that the number of unresolved templates will be different compared to the CWMR approach and have also different sizes for the Gaussian filter sigma as well as the maximum filter spherical radius or $r_{\max}$. Multi-scale images were reconstructed according to Moslemipour et al. [54] by CWMR with sigma = 0.4 and $r_{\max} = 4$ for both rocks, of which porosity and permeability values of the best realization are summarized in Table 2.

To reconstruct images in the OCWMR approach more accurately, we first performed a sensitivity analysis on the porosity and permeability for both rocks on the sigma and $r_{\max}$ parameters. Table 3 summarizes the results of this sensitivity analysis. By comparing the porosity and permeability of multi-scale reconstructed images via the OCWMR with that of the HR image properties (13.7% and 147 mD for the BS rock, and 28.2% and 160 mD for the EBC rock, respectively), it can be concluded that the multi-scale reconstructed images for both rocks with sigma = 0.3 and $r_{\max} = 3$ represent the best match with properties closest to that of the HR image (13.9% and 147 mD for the BS rock, and 27.6% and 161 mD for the EBC rock, respectively). These values are more like that of the HR image than that of the OCWR predictions (summarized in Table 3).

It is worth mentioning that the unresolved porosity should not be divided into too many (sigma = 0.1, $r_{\max} = 1$) or too few segments (sigma = 0.7, $r_{\max} = 7$). If they are divided into too many segments, it will cause the selected templates to become very small and the unresolved templates in LR images will not be adequately replaced. On the other hand, if they are divided into too few segments, it will cause the selected templates to not become best-match templates for the desired template in LR images. This is due to the little overlap of OL with unresolved masks causing a weak connectivity between the added pores. Therefore, sigma = 0.3 and $r_{\max} = 3$ was considered for further computation using the OCWMR.

The number of unresolved templates could have a significant effect on the connectivity created in the multi-scale reconstructed images. As it was mentioned, their optimal number can cause more suitable templates to be selected with an appropriate number of micropores. The number of unresolved templates after applying the watershed algorithm by CWMR with sigma = 0.4 and $r_{\max} = 4$, and OCWMR with sigma = 0.3 and $\mathrm{r}_{\max} = 3$, is shown in Table 4. As evident from this table, the OCWMR approach exhibits a lower number of unresolved templates. This is due to the larger pixel size in the LR image compared to the CWMR approach, resulting in the subdivision of the unresolved phase into larger sections and subsequently reducing the number of unresolved templates.

One key aspect to consider when comparing the OCWMR and CWMR approaches is down-sampling before watershed segmentation. In the OCWMR approach, down-sampling is not performed on the entire LR image and reconstruction is carried out on the Octree structure. On the other hand, the CWMR approach involves down-sampling before watershed segmentation, which can cause changes in the properties of the LR image.

Table 1 Porosity and permeability of the BS and EBC rock samples for both LR and HR images after applying the segmentation

Sample	Porosity (%)			Permeability (mD)	
	LR image		HR image	LR Image	HR image
	Resolved	Unresolved			
BS	12.9	9.3	13.7	170	147
EBC	21.0	22.6	28.2	94	160

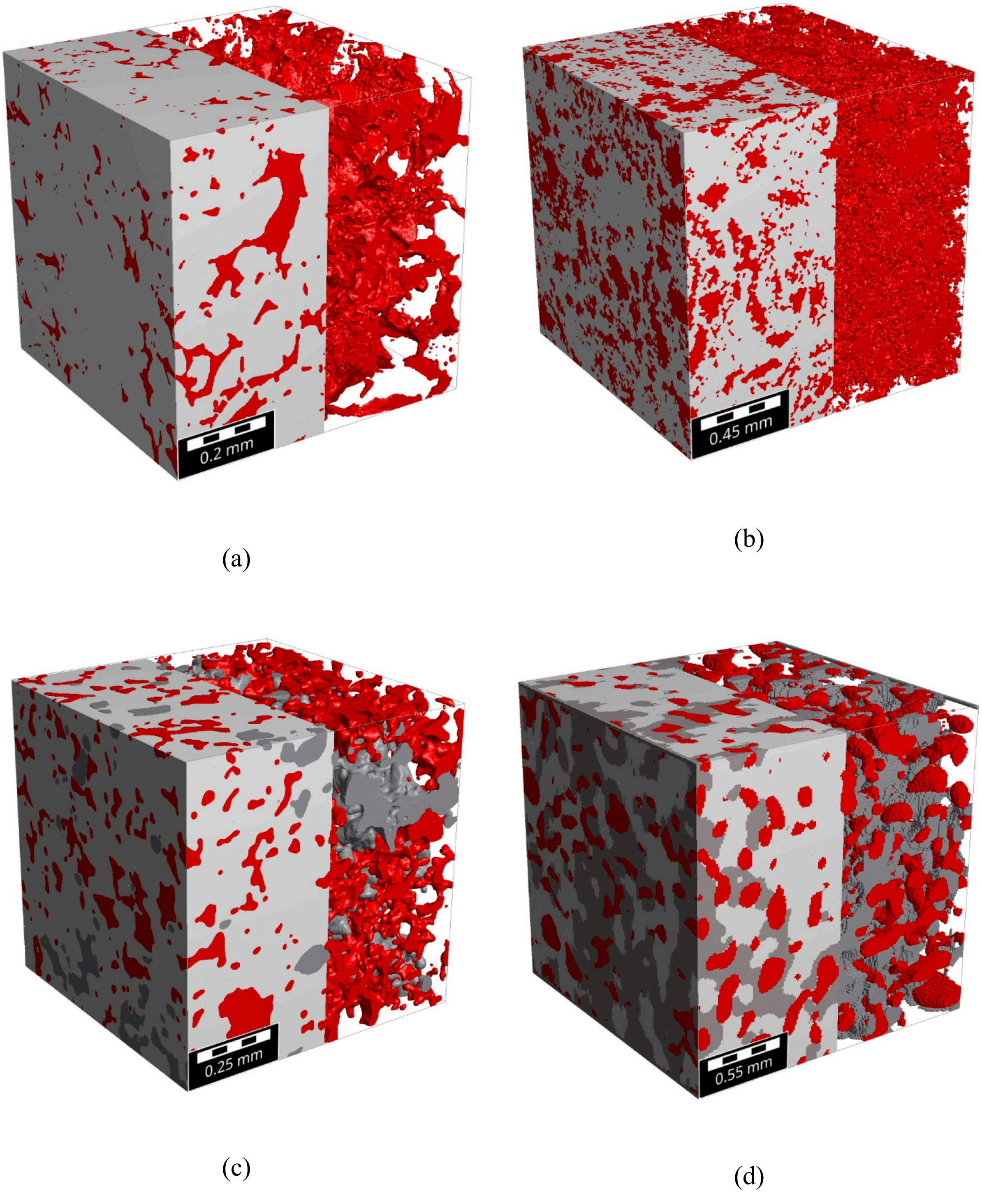

Fig. 8 Segmentation of the HR scan for the (**a**) BS and (**b**) EBC rock samples, along with multi-phase segmentation of the LR scan for the (**c**) BS and (**d**) EBC rock samples. The light gray color pixels in the two lower images show the unresolved porosity

3.4 Computational costs

The muti-scale images of BS and EBC rock samples were reconstructed using the CWMR and OCWMR methods on a workstation equipped with 32 Intel® Xeon® Platinum 8160 2.1 GHz CPU cores and 1 TB of RAM. For the BS

Table 2 Porosity and permeability of multi-scale reconstructed images using CWMR with sigma = 0.4 and $r_{\max} = 4$ for the BS and the EBC rock samples

Sample	Porosity (%)	Permeability (mD)
BS	14.3	141
EBC	27.3	165

Table 3 Sensitivity analysis on sigma and $r_{\max}$ parameters of watershed segmentation method by calculating porosity and permeability in multi-scale images reconstructed by OCWMR

Sigma/$r_{\max}$	BS		EBC	
	Porosity (%)	Permeability (mD)	Porosity (%)	Permeability (mD)
0.1/1	14.6	122	28.1	176
0.2/2	14.4	136	27.9	169
0.3/3	13.9	147	27.6	161
0.4/4	14.1	150	27.5	157
0.5/5	14.3	159	27.7	142
0.6/6	14.4	162	28.2	135
0.7/7	14.6	164	28.5	128
Average	14.3 ± 0.2	149 ± 15	27.9 ± 0.3	153 ± 18

Table 4 The number of unresolved templates for both BS and EBC rock samples after watershed segmentation using CWMR and OCWMR approaches

Sample	Numbers of unresolved templates	
	CWMR	OCWMR
BS	1,797	1,424
EBC	2,080	1,939

rock sample, the CWMR took approximately 120 CPU-h, while OCWMR approach completed the process in around 36 CPU-h, i.e. 3.3 times faster. In the case of the EBC rock sample, the reconstruction processes took approximately 288 and 96 CPU-h to complete (threefold speedup in OCWMR), respectively. Moreover, for the BS multi-scale image reconstruction, the CWMR consumed 65 GB of memory, while OCWMR completed the process by consuming 2.9 GB of memory only, i.e. 22.5 times less. For the EBC multi-scale image reconstruction, the CWMR consumed 276 GB of memory, while OCWMR completed the process by consuming 2.4 GB of memory only, 131.4 times less. Runtime and memory consumption details for image reconstruction methods are summarized in Table 5.

Given the CWMR approach, increasing the number of unresolved templates and subsequently their smaller size could decrease the memory usage and runtime. Therefore, it might be expected that in this context, the OCWMR approach would have a higher memory usage and runtime compared to the CWMR one. However, there is another point that not only increases the memory usage and runtime in the OCWMR approach compared to CWMR but may also significantly reduce both. In the OCWMR approach, watershed segmentation specifically performed to identify various unresolved templates on the LR image with a large voxel size. Moreover, using the Octree structure, only the unresolved templates are computed separately from the rest of the phases in the image. Consequently, this approach involves lower memory usage and runtime than the CWMR. Furthermore, the memory usage and runtime for the EBC rock sample, despite having more unresolved templates, are lower than those for the BS rock sample, contrary to the CWMR approach. This discrepancy is due to the smaller size (voxels) LR image in the EBC rock compared to the LR image of the BS rock. Since the OCWMR approach operates on the LR image, the memory usage and runtime in the EBC rock are less than those in the BS rock. Thus, the OCWMR approach reduces computational cost, addressing one of the significant challenges in previous multi-scale image reconstruction approaches, such as CWMR, especially in rocks with greater resolution differences between LR and HR images.

3.5 Multi-scale image reconstruction using OCWMR

Ten realizations of the multi-scale images were reconstructed for each rock sample using the OCWMR approach. The numbering order of the unresolved templates in each unresolved cluster can start from two directions. In these realizations, the numbering and filling order of the unresolved templates in each cluster is randomly chosen from one of the two directions in each realization, ensuring that the realizations differ from one another. An example of both 3D realization of the multi-scale reconstructed image using OCWMR, and the multi-scale reconstructed image using CWMR, are shown for each rock sample in Fig. 9. Moreover, two random 2D layers of the images are displayed alongside their corresponding LR image layers for comparison purposes. The visual analysis of the images indicates that both approaches have effectively chosen appropriate templates for the unresolved porosity. In both rocks, the reconstructed images by both approaches exhibit small and large pores, and suitable connectivity exists between all pores. The factor that alters the reconstructed multi-scale images using the two methods is the number of unresolved templates. This results from applying the watershed algorithm to LR and down-sampled LR images, as well as using different parameters for watershed segmentation. Therefore, it is expected that there would be differences in the properties of the multi-scale images reconstructed by both approaches. However, since the OCWMR approach has fewer unresolved templates (1,424 and 1,797 for the BS and EBC, respectively) compared to the CWMR (1,939 and 2,080 for the BS and EBC, respectively), it is expected that the number of small pores in the image reconstructed by OCWMR would be somewhat less than CWMR. By comparing the permeability values in Table 2 and Table 3, the OCWMR approach obviously provides results closer to the actual value of the HR image (Table 1). This is due to the higher number of unresolved templates in the CWMR approach, resulting in a larger number of small-size isolated pores and throats that have been added to the image. In addition, greater permeability reduction happened in the BS rock of the multi-scale image reconstructed by the CWMR approach (141 mD). This shows that the added pores by the CWMR approach created more dead-end throats inside the image and couldn't make connectivity closer to the HR image. However, in the multi-scale image reconstructed by the OCWMR approach, this permeability reduction is less and equal to the permeability of the HR image (147 mD). In the EBC rock, the permeability of the image after adding small pores in the CWMR approach has increased (165 mD) because more unnecessary throats have been added, leading to a greater increase in permeability. However, in the multi-scale image reconstructed by the OCWMR approach, the increase in permeability is less and closer (161 mD) to the permeability of the HR image (160 mD).

Furthermore, single- and two-phase flow properties were calculated to assess the quality of the reconstructed images. Figure 10 shows the absolute permeability distribution of the 10 multi-scale images reconstructed using the OCWMR for both the BS and the EBC rock samples. Moreover, to better compare the accuracy of the OCWMR method, the permeability value of the best realization reconstructed using the CWMR method, along with the permeability calculated from the HR image, is displayed in the figure. As evident, the average permeability calculated over 10 reconstructed images by the OCWMR approach shows close agreement to the permeability of the HR images in both rocks. This confirms the accuracy of the proposed approach in multi-scale reconstruction of rock images.

Table 5 Run time and memory consumption of both reconstruction approaches for BS and EBC rock samples

Sample	Run time (CPU-h)		Memory consumption (GB)	
	CWMR	OCWMR	CWMR	OCWMR
BS	120	36	65	2.9
EBC	288	96	276	2.4

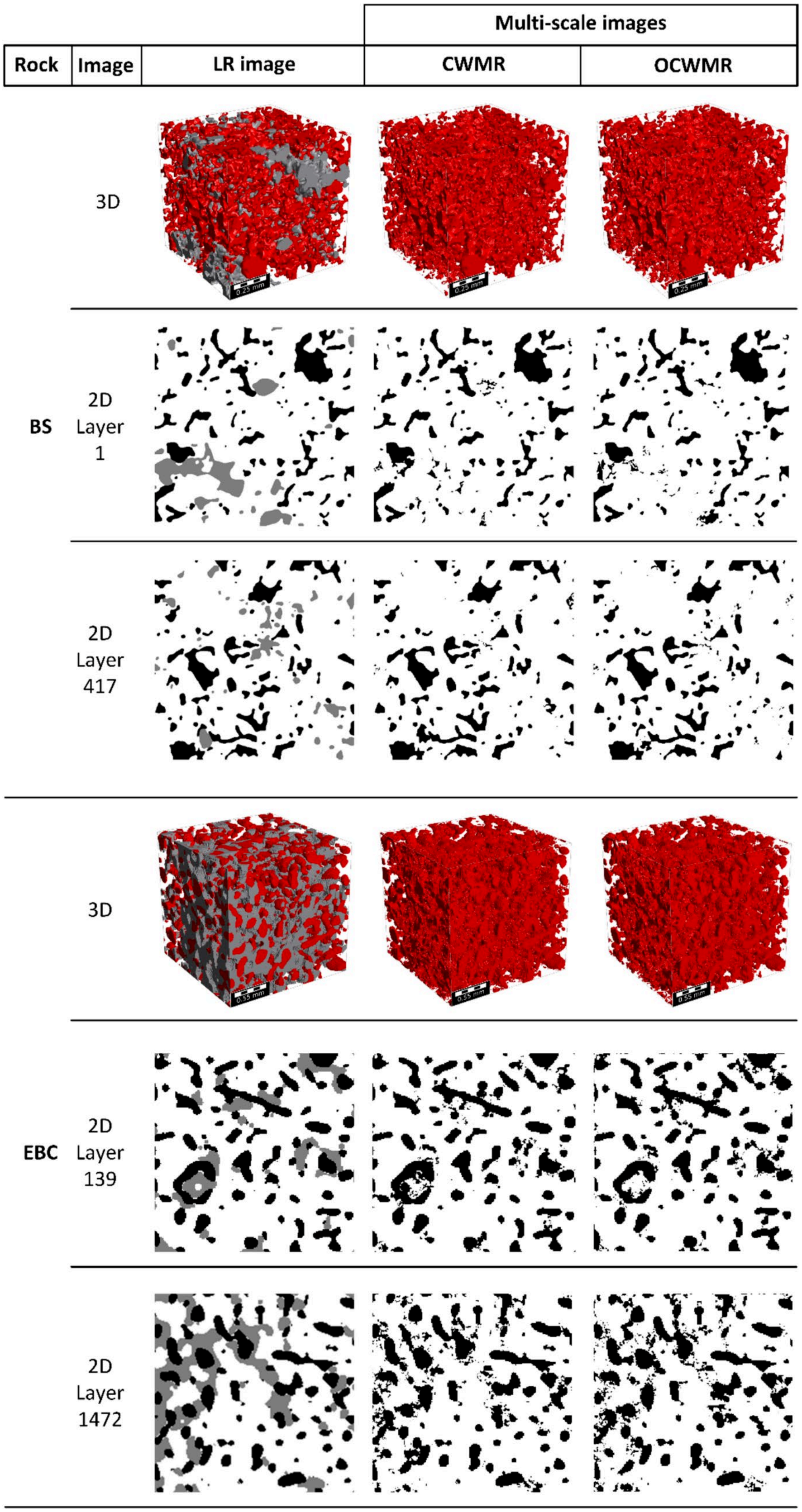

Fig. 9 Multi-scale 3D and 2D images reconstructed using the OCWMR and the CWMR approaches for the BS and EBC rock samples. Some 2D layers of the reconstructed images have been displayed alongside their corresponding layers in the LR image

3.6 Evaluation of two-phase flow properties

We further calculated the properties of the two-phase flow including the capillary pressure and relative permeability curves for both rocks. For this purpose, we considered the 3D realization with best permeability (Fig. 10) for the OCWMR approach to calculate the two-phase flow properties. Figure 11a and b show the capillary pressure curve for the BS and the EBC rocks, respectively. These curves were obtained on the HR image as well as the reconstructed images using the CWMR and the OCWMR approaches. In these simulations, water and air phases have been considered and these curves were obtained during the drainage process. These curves show that in both rocks, the highest capillary pressure value in the image reconstructed using the CWMR is higher than that of the image reconstructed using the OCWMR. This is due to the higher number of small pores existing in the reconstructed images using CWMR and to the inverse relationship between capillary pressure and pore-throat sizes. Moreover, the presence of small pores in the image significantly affects irreducible water saturation, as water becomes trapped in these pores at such saturations. In Fig. 11a, the residual water saturation value of the BS in the OCWMR is lower than that of the CWMR. This shows that in the reconstructed image using the OCWMR method, the number of isolated smaller size pores is lower, and there are fewer dead-end throats. As a result, more water is displaced by air. Therefore, this has caused a better recovery of the water phase in the image compared to the reconstructed image using the CWMR. However, in Fig. 11b, the amount of residual water saturation in the OCWMR is higher than that by the CWMR in the EBC rock. This confirms that in the EBC rock, the presence of smaller pores has caused more connectivity between the pores inside the reconstructed image. Therefore, in the reconstructed image using the CWMR, more water has been recovered due to high connectivity. In addition, in both images, the capillary pressure curve in the HR image is closer to the capillary pressure curve in the image reconstructed using the OCWMR.

Figure 12 a and b show the relative permeability curves for the BS and the EBC rocks, respectively. These curves also were obtained on the HR image as well as on reconstructed images using the CWMR and the OCWMR approaches. In these simulations, water and air phases have been considered, and the curves of the drainage and imbibition processes have been shown. In Fig. 12a, the water relative permeability curve of the image reconstructed using the OCWMR is placed above the image reconstructed using the CWMR in the BS rock. This shows again that the image reconstructed using the CWMR has more isolated smaller size pores

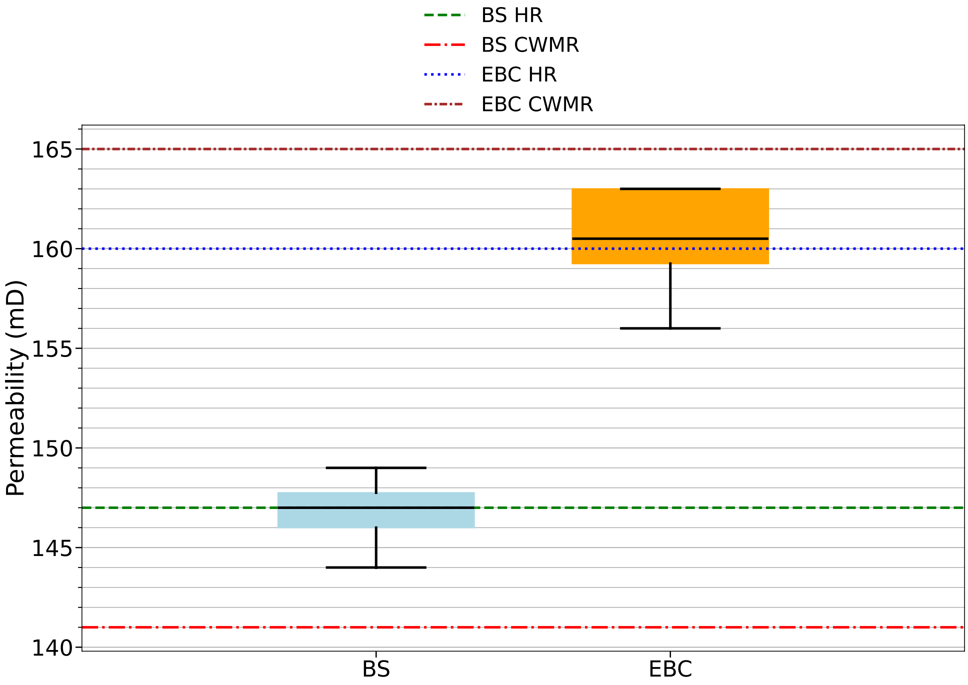

Fig. 10 The permeability distribution of all 10 multi-scale image realizations reconstructed using the OCWMR for the BS and the EBC rock samples

Fig. 11 The capillary pressure curves of the HR image as well as reconstructed images using the OCWMR and the CWMR approaches for (**a**) the BS and (**b**) the EBC rock sample

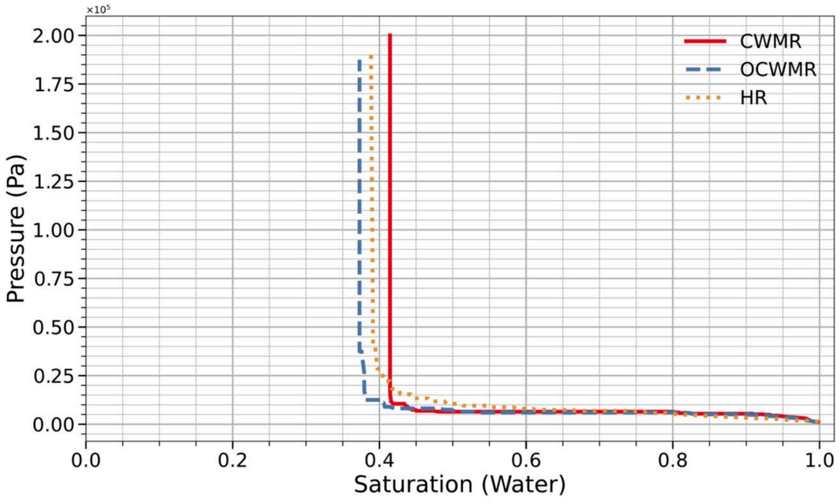

(a)

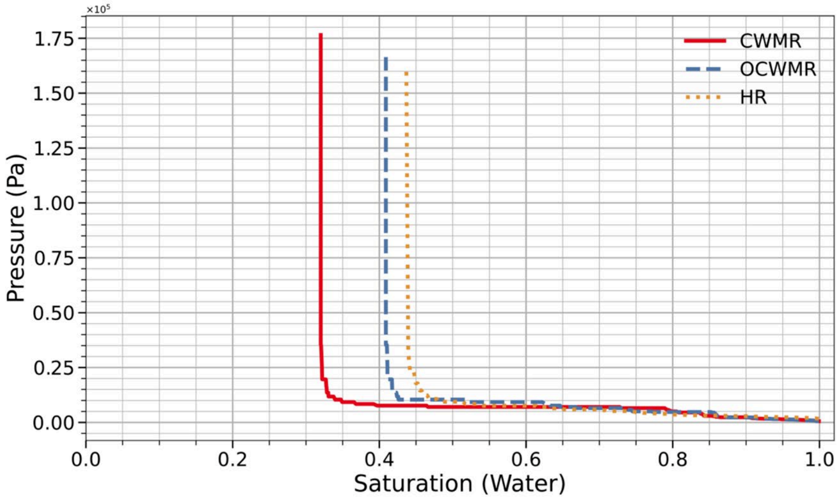

(b)

and dead-end throats. Therefore, the water relative permeability values have more reductions at higher water saturations. However, in Fig. 12b for the EBC rock, the water relative permeability curve in the image reconstructed using the OCWMR is lower than that of the reconstructed image by the CWMR at higher water saturations. This shows the greater effect of smaller size pores in increasing the permeability in the reconstructed image using the CWMR by improving the connectivity between the larger size pores. Moreover, the presence of small pores in the image significantly impacts the relative permeability curve during the drainage process, particularly at saturations close to the irreducible water saturation. At these saturations, water becomes trapped in small pores, influencing the air relative permeability. In the multi-scale image reconstructed using the CWMR method, the presence of more small pores and greater connectivity (i.e., both among these pores and with resolved pores) causes the shape of the air relative permeability curve, especially at saturations near irreducible water saturation, to deviate from the actual rock behavior. However, in the OCWMR method, the reconstructed multi-scale image more accurately reflects the rock's real structure. Small pores and their connectivity are better represented, resulting in an air relative permeability curve that more closely matches that of the HR image. Therefore, for both rocks the relative permeability curves in the HR image are closer to the relative permeability curves in the image reconstructed using the OCWMR.

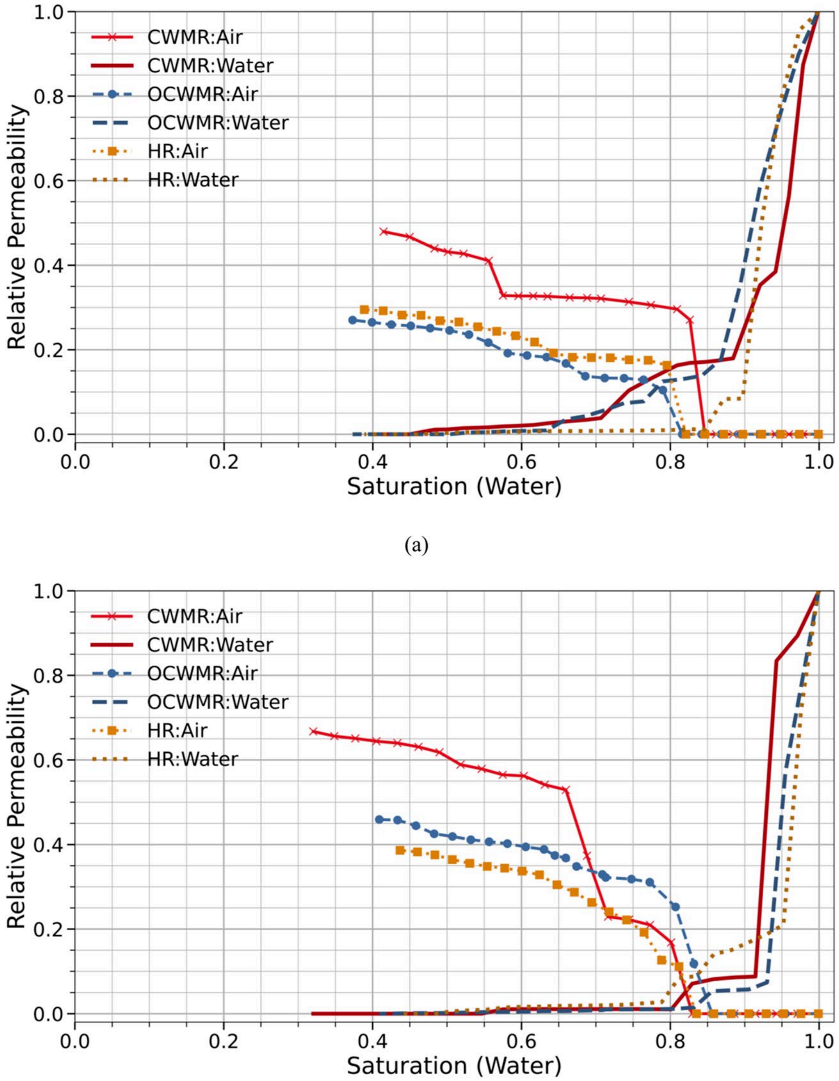

Fig. 12 The relative permeability curves of the HR image as well as reconstructed images using the OCWMR and the CWMR approaches for (**a**) the BS and (**b**) the EBC rock samples

(a)

(b)

3.7 Discussion

The CWMR and OCWMR methods have three key differences that result in lower computational cost and higher accuracy for the OCWMR method compared to the CWMR method. In the CWMR method, segmentation is performed on the down-sampled LR image with a fine voxel size, whereas in the OCWMR method, segmentation is applied directly to the LR image with a coarse voxel size. Since the segmentation in OCWMR is applied to the original LR image, the number of unresolved templates is more optimal than in the CWMR method. Additionally, the OCWMR method utilizes optimized parameters for watershed segmentation (sigma and r_{max}), ensuring that the number of unresolved templates is as close to optimal as possible. An optimal number of unresolved templates allows for better-matching templates to be selected for replacement in the LR image. If the number of unresolved templates is lower than optimal, their size increases, causing the selected OL region to shift away from the unresolved mask within the unresolved template. This misalignment disrupts the effectiveness of the CCF equation, leading to suboptimal template selection from the HR image. As a result, template selection becomes somewhat random, increasing the likelihood of excessive small-sized pores and poor connectivity in the reconstructed multi-scale image. Conversely, if the number of unresolved templates exceeds the optimal amount, their size decreases, leading to a smaller OL area. A reduced OL area also restricts the effectiveness of the CCF equation, preventing the selection of appropriate templates from the HR image. Like the previous case, this increases the probability of excessive small-sized pores and poor connectivity in the reconstructed multi-scale image. Moreover, since the selected templates from the HR image do not establish proper connectivity in the reconstructed multi-scale image, this method has a higher likelihood of containing isolated small-sized pores and dead-end throats.

Beyond the differences in watershed segmentation applied to LR images with different voxel sizes, the two methods also employ distinct structures for multi-scale image reconstruction. In the OCWMR method, after watershed segmentation, only the unresolved templates in the LR image are down-sampled, while the voxel size in the remaining areas remains coarse, forming an Octree structure. In contrast, the CWMR method down-samples the entire LR image. As a result, in the OCWMR method, the CCF equation is solved within the Octree structure for each unresolved template, significantly reducing memory consumption and runtime. This distinction leads to a substantial difference in computational cost, particularly in memory usage. The difference is even more pronounced in cases where the resolution difference between the LR and HR images is large, such as in EBC rock.

The most significant advantage of our novel OCWMR method is its reduction in memory usage and runtime. This reduction in computational cost becomes even more pronounced when the resolution difference between the LR and HR images is higher, highlighting the benefits of using the Octree technique for multi-scale image reconstruction. However, a disadvantage of this method is that the resolution difference between images must be a power of 2 (i.e., 2^n), often requiring image resampling. Developing a method that overcomes this disadvantage could be an interesting topic for future research.

4 Summary and conclusions

In this study, we compared the predicted geometric property (porosity) as well as single-phase (permeability) and two-phase (capillary pressure, relative permeability) flow properties obtained using the novel OCWMR and the conventional CWMR approaches. The findings are summarized as follows:

- Our results indicate that the novel OCWMR approach yields properties that are closer to those derived from HR images. This improvement is attributed to the use of optimal parameters in the watershed segmentation algorithm and applying it directly to the LR image with a coarse voxel size, resulting in higher accuracy due to fewer unresolved templates.
- The reconstructed multi-scale images using the novel OCWMR effectively capture the properties of the HR images.
- The number of unresolved templates differed slightly between the OCWMR and CWMR approaches. This difference was crucial for aligning the properties closer to those of the HR image.
- Our novel OCWMR approach resulted in fewer unresolved templates. Consequently, it added fewer isolated small pores and dead-end throats to the BS image. Conversely, it added fewer unnecessary small-size pores and throats to the EBC image compared to the conventional CWMR approach.
- Fewer unresolved templates in the OCWMR approach led to a smaller permeability reduction and residual water saturation value in the BS rock. It also caused a smaller increase in permeability and larger residual water saturation value in the EBC rock.
- Additionally, our novel OCWMR approach significantly reduced computational cost and runtime compared to the conventional CWMR approach. This was especially more pronounced for images with greater resolution differences between LR and HR images. Thus, the OCWMR approach is more efficient and thus of practical use for multi-scale image reconstruction in rock property prediction.

In this research, certain assumptions were made. These assumptions can be explored further in future studies. First, the results were validated using HR image properties at the REV size. Future studies may use laboratory data for more sophisticated validation. Additionally, the same region of interest can be scanned at HR and LR to enable better comparison. While this study focused on sandstone and carbonate rocks, future work can include rocks (e.g., shales), which have a wider range of pore sizes. In such heterogeneous rocks, pore sizes can be spread at several scales. Thus, various scans at multiple resolutions (greater than two) can be integrated together to reconstruct a multiscale image, making it an interesting topic for future research.

Nomenclatures FoV: Field of View; REV: Representative Elementary Volume; DRP: Digital Rock Physics; BS: Berea sandstone; EBC: Edward Brown Carbonate; HR: High-resolution; LR: Low-resolution; OL: Overlap region; µXCT: X-ray computer microtomography; CCSIM: Cross-correlation Based Simulation; CCF: Cross-correlation Function; CWMR: CCSIM Watershed-based Multi-scale Reconstruction; OCWMR: Octree-based Watershed Multi-scale Reconstruction; LIR: Left-Identity-Right; C: Cross-correlation function value; DI: The main domain or HR image; D_t: The data event; $w^{'}$: Width of overlap region; ϕ: Porosity; K: Permeability; Kr: Relative Permeability; ΔP_c: Capillary Pressure; IFT: Interfacial Tension

Acknowledgements The first author (A.M.) gratefully acknowledges financial support from the DAAD (German Academic Exchange Service). We acknowledge DESY (Hamburg, Germany), a member of the Helmholtz Association HGF, for the provision of experimental facilities. Parts of this research were carried out at the PETRA III synchrotron facility, and we would like to thank Dr. Fabian Wilde for assistance in using the photon imaging beamline HEREON IBL P05. The fifth (T.S.) author acknowledges the financial support from the German Science Foundation for the acquisition of a micro-CT scanner under grant number DFG- 411334776.

Author contributions Conceptualization: Saeid Sadeghnejad; Abolfazl Moslemipour; Methodology: Abolfazl Moslemipour, Saeid Sadeghnejad, Frieder Enzmann; Formal analysis and investigation: Abolfazl Moslemipour, Saeid Sadeghnejad, Frieder Enzmann, Michael Kersten; Writing—original draft preparation: Abolfazl Moslemipour; Writing—review and editing: Abolfazl Moslemipour, Saeid Sadeghnejad, Frieder Enzmann, Michael Kersten, Davood Khoozan, Thorsten Schaefer; Funding acquisition: Abolfazl Moslemipour, Saeid Sadeghnejad, Frieder Enzmann, Thorsten Schäfer; Resources: Saeid Sadeghnejad, Frieder Enzmann, Thorsten Schäfer; Supervision: Saeid Sadeghnejad, Frieder Enzmann, Michael Kersten, Davood Khoozan.

Funding Open Access funding enabled and organized by Projekt DEAL.

Data and code availability All data that supports the findings of this study are available from the corresponding author upon reasonable request. Moreover, the source code used in this study is available on GitHub at https://github.com/Abolfazlmsl/Octree-based-watershed-Multi-scale-Reconstruction and https://github.com/Saeid-Sli/Octree-based-watershed-Multi-scale-Reconstruction.

Declarations Abolfazl Moslemipour reports financial support was provided by German Academic Exchange Service (DAAD). Other authors declare that they have no known competing financial interests or personal relationships that could have appeared to influence the work reported in this paper.

References

1. Bultreys, T., Stappen, J.V., Kock, T.D., Boever, W.D., Boone, M.A., Hoorebeke, L.V., Cnudde, V.: Investigating the relative permeability behavior of microporosity-rich carbonates and tight sandstones with multiscale pore network models. J. Geophys. Res.: Solid. Earth. **121**(11), 7929–7945 (2016). https://doi.org/10.1002/2016JB013328
2. Sadeghnejad, S., Ashrafizadeh, M., Nourani, M.: Improved oil recovery by gel technology: Water shutoff and conformance control. In: Chemical Methods, pp. 249–312. Elsevier (2022)
3. Koochakzadeh, A., Ashrafizadeh, M., Masoudi, M., Sadeghnejad, S., Schäfer, T.: *Application of pH-Sensitive Microgels as an EOR Agent: Rheological and Reservoir Mobility Control Evaluation*. in *85th EAGE Annual Conference &*

Exhibition (including the Workshop Programme). 2024. European Association of Geoscientists & Engineers. https://doi.org/10.3997/2214-4609.202410838.

4. Ashrafizadeh, M., Abdollahi, M., Javadi, A., Tam, K.C.: Cross-linked amphiphilic polyelectrolyte colloidal gels: green synthesis and chemical and microstructure analysis. Mater. Today. Chem. **36**, 101893 (2024). https://doi.org/10.1016/j.mtchem.2023.101893
5. Karsanina, M.V., Gerke, K.M., Skvortsova, E.B., Ivanov, A.L., Mallants, D.: Enhancing image resolution of soils by stochastic multiscale image fusion. Geoderma **314**, 138–145 (2018). https://doi.org/10.1016/j.geoderma.2017.10.055
6. Koochakzadeh, A., Teimouri, A., Tohidi, E., Ashrafizadeh, M., Enzmann, F., Kersten, M., Sadeghnejad, S.: Review on using pH-sensitive microgels as enhanced oil recovery and water shutoff agents: concepts, recent developments, and future challenges. Geoenergy. Sci. Eng. **223**, 211477 (2023). https://doi.org/10.1016/j.geoen.2023.211477
7. Hogeweg, S., Strobel, G., Hagemann, B.: Benchmark study for the simulation of underground hydrogen storage operations. Comput. Geosci. **26**(6), 1367–1378 (2022). https://doi.org/10.1007/s10596-022-10163-5
8. Esfandi, T., Sadeghnejad, S., Jafari, A.: Effect of reservoir heterogeneity on well placement prediction in CO2-EOR projects using machine learning surrogate models: benchmarking of boosting-based algorithms. Geoenergy Sci. Eng. **233**, 212564 (2024). https://doi.org/10.1016/j.geoen.2023.212564
9. Qin, Z., Arshadi, M., Piri, M.: Near-miscible supercritical CO2 injection in oil-wet carbonate: a pore-scale experimental investigation of wettability state and three-phase flow behavior. Adv. Water. Resour. **158**, 104057 (2021). https://doi.org/10.1016/j.advwatres.2021.104057
10. Sadeghnejad, S., Enzmann, F., Kersten, M.: Digital rock physics, chemistry, and biology: challenges and prospects of pore-scale modelling approach. Appl. Geochem. **131**, 105028 (2021). https://doi.org/10.1016/j.apgeochem.2021.105028
11. Liu, Y., Chen, M., Sun, S., Lei, Z., Zeng, J., Cai, J.: Effects of grain shape and packing pattern on spontaneous imbibition under different boundary conditions: pore-scale simulation. J. Hydrol. **607**, 127484 (2022). https://doi.org/10.1016/j.jhydrol.2022.127484
12. McClure, J.E., Ramstad, T., Li, Z., Armstrong, R.T., Berg, S.: Modeling geometric state for fluids in porous media: evolution of the euler characteristic. Transp. Porous. Media. **133**, 229–250 (2020). https://doi.org/10.1007/s11242-020-01420-1
13. Prodanović, M., Lindquist, W., Seright, R.: 3D image-based characterization of fluid displacement in a berea core. Adv. Water. Resour. **30**(2), 214–226 (2007). https://doi.org/10.1016/j.advwatres.2005.05.015
14. Song, W., Wang, D., Yao, J., Li, Y., Sun, H., Yang, Y., Zhang, L.: Multiscale image-based fractal characteristic of shale pore structure with implication to accurate prediction of gas permeability. Fuel **241**, 522–532 (2019). https://doi.org/10.1016/j.fuel.2018.12.062
15. Tahmasebi, P.: Nanoscale and multiresolution models for shale samples. Fuel **217**, 218–225 (2018). https://doi.org/10.1016/j.fuel.2017.12.107
16. Li, R., Hou, X., Chen, L., Fang, H., Zheng, C.: Multifractal investigation on multi-scale pore structure heterogeneity of high rank coal reservoirs. Nat. Resour. Res. **31**(3), 1665–1685 (2022). https://doi.org/10.1007/s11053-022-10046-7
17. Bal, A., Misra, S., Sen, D.: Nanopore heterogeneity and accessibility in oil and gas bearing cretaceous KG (Raghampuram) shale, KG basin, India: an advanced multi-analytical study. Nat. Resour. Res. **33**(3), 1131–1154 (2024). https://doi.org/10.1007/s11053-024-10319-3
18. Moslemipour, A., Sadeghnejad, S.: Dual-scale pore network reconstruction of vugular carbonates using multi-scale imaging techniques. Adv. Water. Resour. **147**, 103795 (2021). https://doi.org/10.1016/j.advwatres.2020.103795
19. Henares, S., Caracciolo, L., Cultrone, G., Fernández, J., Viseras, C.: The role of diagenesis and depositional facies on pore system evolution in a triassic outcrop analogue (SE Spain). Mar. Pet. Geol. **51**, 136–151 (2014). https://doi.org/10.1016/j.marpetgeo.2013.12.004
20. Chen, Z., Zhu, C-Y., Yu, B., Gong, L.: *Pore-scale study on the permeability characteristics of fractured rock under hydraulic-chemical coupling*. Compu. Geosci. (2024) p. 1–12. https://doi.org/10.1007/s10596-024-10308-8.
21. Huang, J., Wang, L., Liu, X.: Lattice Boltzmann method for solute transport in dual-permeability media. J. Hydrol. **619**, 129339 (2023). https://doi.org/10.1016/j.jhydrol.2023.129339
22. Moslemipour, A., Sadeghnejad, S., Enzmann, F., Khoozan, D., Hupfer, S., Schäfer, T., Kersten, M.: *Multi-Scale Pore Network Fusion and Upscaling of Microporosity Using Artificial Neural Network*. Marine and Petroleum Geology, 2025: p. 107349. https://doi.org/10.1016/j.marpetgeo.2025.107349.
23. Mehmani, A., Verma, R., Prodanović, M.: Pore-scale modeling of carbonates. Mar. Pet. Geol. **114**, 104141 (2020). https://doi.org/10.1016/j.marpetgeo.2019.104141
24. Raeini, A.Q., Yang, J., Bondino, I., Bultreys, T., Blunt, M.J., Bijeljic, B.: Validating the generalized pore network model using micro-CT images of two-phase flow. Transp. Porous. Media. **130**(2), 405–424 (2019). https://doi.org/10.1007/s11242-019-01317-8
25. Gostick, J., Aghighi, M., Hinebaugh, J., Tranter, T., Hoeh, M.A., Day, H., Spellacy, B., Sharqawy, M.H., Bazylak, A., Burns, A.: Open PNM: a pore network modeling package. Comput. Sci. Eng. **18**(4), 60–74 (2016). https://doi.org/10.1109/MCSE.2016.49
26. Gostick, J.T.: Versatile and efficient pore network extraction method using marker-based watershed segmentation. Phys. Rev. E. **96**(2), 023307 (2017). https://doi.org/10.1103/PhysRevE.96.023307

27. Lindquist, W.B., Lee, S.M., Coker, D.A., Jones, K.W., Spanne, P.: Medial axis analysis of void structure in three-dimensional tomographic images of porous media. J. Geophys. Res.: Solid. Earth. **101**(B4), 8297–8310 (1996). https://doi.org/10.1029/95JB03039
28. Silin, D., Patzek, T.: Pore space morphology analysis using maximal inscribed spheres. Phys. A. **371**(2), 336–360 (2006). https://doi.org/10.1016/j.physa.2006.04.048
29. Jiang, Z., Van Dijke, M., Wu, K., Couples, G.D., Sorbie, K.S., Ma, J.: Stochastic pore network generation from 3D rock images. Transp. Porous. Media. **94**, 571–593 (2012). https://doi.org/10.1007/s11242-011-9792-z
30. Prodanović, M., Mehmani, A., Sheppard, A.P.: *Imaged-based multiscale network modelling of microporosity in carbonates.* (2015)
31. Sadeghnejad, S., Gostick, J.: Multiscale reconstruction of vuggy carbonates by pore-network modeling and image-based technique. SPE. J. **25**(01), 253–267 (2020). https://doi.org/10.2118/198902-PA
32. Bultreys, T., Van Hoorebeke, L., Cnudde, V.: Multi-scale, micro-computed tomography-based pore network models to simulate drainage in heterogeneous rocks. Adv. Water. Resour. **78**, 36–49 (2015). https://doi.org/10.1016/j.advwatres.2015.02.003
33. Lin, W., Li, X., Yang, Z., Manga, M., Fu, X., Xiong, S., Gong, A., Chen, G., Li, H., Pei, L.: Multiscale digital porous rock reconstruction using template matching. Water. Resour. Res. **55**(8), 6911–6922 (2019). https://doi.org/10.1029/2019WR025219
34. Ruspini, L., Øren, P., Berg, S., Masalmeh, S., Bultreys, T., Taberner, C., Sorop, T., Marcelis, F., Appel, M., Freeman, J.: Multiscale digital rock analysis for complex rocks. Transp. Porous. Media. **139**(2), 301–325 (2021). https://doi.org/10.1007/s11242-021-01667-2
35. Yan, P., Teng, Q., Ma, Z., Wu, X., He, X.: Modeling finer microstructure of random heterogeneous porous materials by fusing 2D high-and 3D low-resolution images. Comput. Geotech. **168**, 106145 (2024). https://doi.org/10.1016/j.compgeo.2024.106145
36. Chi, P., Sun, J., Yan, W., Luo, X.: Multiscale fusion of tight sandstone digital rocks using attention-guided generative adversarial network. Mar. Pet. Geol. **160**, 106647 (2024). https://doi.org/10.1016/j.marpetgeo.2023.106647
37. Zheng, Q., Zhang, D.: RockGPT: reconstructing three-dimensional digital rocks from single two-dimensional slice with deep learning. Comput. Geosci. **26**(3), 677–696 (2022). https://doi.org/10.1007/s10596-022-10144-8
38. Xu, Z., Lin, M., Jiang, W., Ji, L., Xu, L., Cao, G.: A pore network-based multiscale coupled model for rapid permeability prediction of tight sandstone gas. Mar. Pet. Geol. **160**, 106600 (2024). https://doi.org/10.1016/j.marpetgeo.2023.106600
39. Zhang, L., Guo, B., Qin, C., Xiong, Y.: *A hybrid pore-network-continuum modeling framework for flow and transport in 3D digital images of porous media.* Adv. Water. Resour. (2024): p. 104753. https://doi.org/10.1016/j.advwatres.2024.104753
40. JamshidiGohari, M.S., EmamiNiri, M., Sadeghnejad, S., Ghiasi-Freez, J.: An ensemble-based machine learning solution for imbalanced multiclass dataset during lithology log generation. Sci. Rep. **13**(1), 21622 (2023). https://doi.org/10.1038/s41598-023-49080-7
41 JamshidiGohari, M.S., Niri, M.E., Sadeghnejad, S., Ghiasi-Freez, J.: Synthetic graphic well log generation using an enhanced deep learning workflow: imbalanced multiclass data, sample size, and scalability challenges. SPE. J. **29**(01), 1–20 (2024). https://doi.org/10.2118/217466-PA
42. Mousavi, S.M., Bakhtiarimanesh, P., Enzmann, F., Kersten, M., Sadeghnejad, S.: Machine-learned surrogate models for efficient oil well placement under operational reservoir constraints. SPE. J. **29**(01), 518–537 (2024). https://doi.org/10.2118/217467-PA
43. Zhang, T., Dong, Y., Bai, H., Peng, Y.: Stochastic reconstruction of shale combining multi-scale generators and discriminators with attention mechanisms. Comput. Geosci. **27**(6), 1041–1065 (2023). https://doi.org/10.1007/s10596-023-10249-8
44. Zhang, T., Li, D., Lu, F.: A pore space reconstruction method of shale based on autoencoders and generative adversarial networks. Comput. Geosci. **25**, 2149–2165 (2021). https://doi.org/10.1007/s10596-021-10083-w
45. Guo, F.-Q., Zhang, H., Yang, Z.-J., Huang, Y.-J., Withers, P.J.: A spherical harmonic-random field coupled method for efficient reconstruction of CT-image based 3D aggregates with controllable multiscale morphology. Comput. Methods. Appl. Mech. Eng. **406**, 115901 (2023). https://doi.org/10.1016/j.cma.2023.115901
46. Costa, T.B., Kennedy, K., Peszynska, M.: Hybrid three-scale model for evolving pore-scale geometries. Comput. Geosci. **22**, 925–950 (2018). https://doi.org/10.1007/s10596-018-9733-9
47. Okabe, H. Blunt, M.J.: *Pore space reconstruction of vuggy carbonates using microtomography and multiple-point statistics.* Water. Resources. Res. **43**(12) (2007). https://doi.org/10.1029/2006WR005680.
48. Tahmasebi, P., Javadpour, F., Sahimi, M.: Multiscale and multiresolution modeling of shales and their flow and morphological properties. Sci. Rep. **5**(1), 1–11 (2015). https://doi.org/10.1038/srep16373
49. Li, X., Teng, Q., Zhang, Y., Xiong, S., Feng, J.: Three-dimensional multiscale fusion for porous media on microtomography images of different resolutions. Phys. Rev. E. **101**(5), 053308 (2020). https://doi.org/10.1103/PhysRevE.101.053308
50. Jacob, A., Enzmann, F., Hinz, C., Kersten, M.: Analysis of variance of porosity and heterogeneity of permeability at the pore scale. Transp. Porous. Media. **130**(3), 867–887 (2019). https://doi.org/10.1007/s11242-019-01342-7
51. Jacob, A., Peltz, M., Hale, S., Enzmann, F., Moravcova, O., Warr, L.N., Grathoff, G., Blum, P., Kersten, M.: Simulating permeability reduction by clay mineral nanopores in a tight sandstone by combining µXCT and FIB-SEM imaging. Solid. Earth. Discuss. **2020**(2020), 1–28 (2021). https://doi.org/10.5194/se-12-1-2021

52. Wang, Y., Arns, J.-Y., Rahman, S.S., Arns, C.H.: Three-dimensional porous structure reconstruction based on structural local similarity via sparse representation on micro-computed-tomography images. Phys. Rev. E **98**(4), 043310 (2018). https://doi.org/10.1103/PhysRevE.98.043310
53. Wu, Y., Tahmasebi, P., Lin, C., Ren, L., Dong, C.: Multiscale modeling of shale samples based on low-and high-resolution images. Mar. Pet. Geol. **109**, 9–21 (2019)
54. Moslemipour, A., Sadeghnejad, S., Enzmann, F., Khoozan, D., Hupfer, S., Schäfer, T., Kersten, M.: Image-based multiscale reconstruction of unresolved microporosity in 3D heterogeneous rock digital twins using cross-correlation simulation and watershed algorithm. Transport. Porous. Media. (2024). https://doi.org/10.1007/s11242-024-02111-x
55 Sadeghnejad, S., Reinhardt, M., Enzmann, F., Arnold, P., Brandstätter, B., Wilde, F., Hupfer, S., Schäfer, T., Kersten, M.: Minkowski functional evaluation of representative elementary volume of rock microtomography images at multiple resolutions. Adv. Water. Resour. **179**, 104501 (2023). https://doi.org/10.1016/j.advwatres.2023.104501
56. Moosmann, J., Ershov, A., Weinhardt, V., Baumbach, T., Prasad, M.S., LaBonne, C., Xiao, X., Kashef, J., Hofmann, R.: Time-lapse x-ray phase-contrast microtomography for in vivo imaging and analysis of morphogenesis. Nat. Protoc. **9**(2), 294–304 (2014). https://doi.org/10.1038/nprot.2014.033
57. Schofield, R., King, L., Tayal, U., Castellano, I., Stirrup, J., Pontana, F., Earls, J., Nicol, E.: Image reconstruction: part 1–understanding filtered back projection, noise and image acquisition. J. Cardiovasc. Comput. Tomogr. **14**(3), 219–225 (2020). https://doi.org/10.1016/j.jcct.2019.04.008
58. Tayal, U., King, L., Schofield, R., Castellano, I., Stirrup, J., Pontana, F., Earls, J., Nicol, E.: Image reconstruction in cardiovascular CT: part 2–Iterative reconstruction; potential and pitfalls. J. Cardiovasc. Comput. Tomogr. **13**(3), 3–10 (2019). https://doi.org/10.1016/j.jcct.2019.04.009
59. Willemink, M.J., Noël, P.B.: The evolution of image reconstruction for CT—from filtered back projection to artificial intelligence. Eur. Radiol. **29**, 2185–2195 (2019). https://doi.org/10.1007/s00330-018-5810-7
60 Abu Anas, E.M., Kim, J.G., Lee, S.Y., Hasan, M.K.: Comparison of ring artifact removal methods using flat panel detector based CT images. Biomed. Eng. Online. **10**, 1–25 (2011). https://doi.org/10.1186/1475-925X-10-72
61. Fu, T., Wang, Y., Zhang, K., Zhang, J., Wang, S., Huang, W., Yao, C., Zhou, C., Yuan, Q.: Deep-learning-based ring artifact correction for tomographic reconstruction. Synchrotron. Radiat. **30**(3), 620–626 (2023). https://doi.org/10.1107/s1600577523000917
62. Reinhardt, M., Jacob, A., Sadeghnejad, S., Cappuccio, F., Arnold, P., Frank, S., Enzmann, F., Kersten, M.: Benchmarking conventional and machine learning segmentation techniques for digital rock physics analysis of fractured rocks. Environ. Earth. Sci. **81**(3), 71 (2022). https://doi.org/10.1007/s12665-021-10133-7
63. Ronneberger, O., Fischer, P., Brox, T.: U-net: convolutional networks for biomedical image segmentation. In: Medical image computing and computer-assisted intervention–MICCAI 2015: 18th international conference, Munich, Germany, October 5–9, (2015) proceedings, part III 18, pp. 234–241. Springer International Publishing (2015). https://doi.org/10.1007/978-3-319-24574-4_28
64. Jackins, C.L., Tanimoto, S.L.: Oct-trees and their use in representing three-dimensional objects. Comput. Graphics. Image. Process. **14**(3), 249–270 (1980)
65. Jayaraman, P.K., Mei, J., Cai, J., Zheng, J.: Quadtree convolutional neural networks. In: Proceedings of the European conference on computer vision (ECCV), pp. 546–561. (2018). https://doi.org/10.1007/978-3-030-01231-1_34
66. Wang, P.-S., Liu, Y., Guo, Y.-X., Sun, C.-Y., Tong, X.: O-cnn: Octree-based convolutional neural networks for 3d shape analysis. ACM Trans. Graph. (TOG) **36**(4), 1–11 (2017). https://doi.org/10.48550/arXiv.1712.01537
67. Zhang, J., Eisenträger, S., Zhan, Y., Saputra, A., Song, C.: Direct point-cloud-based numerical analysis using octree meshes. Comput. Struct. **289**, 107175 (2023). https://doi.org/10.1016/j.compstruc.2023.107175
68. Linden, S., Wiegmann, A., Hagen, H.: The LIR space partitioning system applied to the Stokes equations. Graph. Models **82**, 58–66 (2015)
69. Linden, S., Hagen, H., Wiegmann, A.: The LIR space partitioning system applied to Cartesian grids. In: International Conference on Mathematical Methods for Curves and Surfaces, pp. 324–340. Springer Berlin Heidelberg, Heidelberg (2012). https://doi.org/10.1007/978-3-642-54382-1_19
70. Hilpert, M., Miller, C.T.: Pore-morphology-based simulation of drainage in totally wetting porous media. Adv. Water. Resour. **24**(3–4), 243–255 (2001). https://doi.org/10.1016/S0309-1708(00)00056-7
71. Schulz, V.P., Wargo, E.A., Kumbur, E.C.: Pore-morphology-based simulation of drainage in porous media featuring a locally variable contact angle. Transp. Porous. Media. **107**, 13–25 (2015). https://doi.org/10.1007/s11242-014-0422-4
72. Arnold, P., Dragovits, M., Linden, S., Hinz, C., Ott, H.: Forced imbibition and uncertainty modeling using the morphological method. Adv. Water. Resour. **172**, 104381 (2023). https://doi.org/10.1016/j.advwatres.2023.104381
73. Singh, A., Regenauer-Lieb, K., Walsh, S.D., Armstrong, R.T., van Griethuysen, J.J., Mostaghimi, P.: On representative elementary volumes of grayscale micro-CT images of porous media. Geophys. Res. Lett. **47**(15), e2020GL088594 (2020)

Authors and Affiliations

Abolfazl Moslemipour[1,3] · **Saeid Sadeghnejad**[2] · **Frieder Enzmann**[1] · **Davood Khoozan**[3] · **Thorsten Schäfer**[2] · **Michael Kersten**[1]

✉ Saeid Sadeghnejad
s.sadeghnejad@uni-jena.de

Thorsten Schäfer
thorsten.schaefer@uni-jena.de

[1] Geosciences Institute, Johannes Gutenberg-University, 55099 Mainz, Germany

[2] Applied Geology, Institute for Geosciences, Friedrich-Schiller-University Jena, 07749 Jena, Germany

[3] Department of Petroleum Engineering, Faculty of Chemical Engineering, Tarbiat Modares University, Tehran, Iran